# PATIENT-SPECIFIC COLLISION ZONES FOR $4\pi$ TRAJECTORY OPTIMIZED RADIATION THERAPY

by

Cassidy Northway

Submitted in partial fulfillment of the requirements
for the degree of Master of Science

at

Dalhousie University
Halifax, Nova Scotia
August 2020

## Table of Contents

# List of Tables

# List of Figures

# Abstract

This thesis presents a system that determined patient-specific collision zones (CZs) to enable safe and deliverable non-coplanar treatment trajectories for stereotactic body radiation therapy (SBRT) patients. Full body scans of patients in treatment position were acquired using an optical scanner, creating a library of scans to augment CT scans. This resulted in a patient model that was aligned with a model of the treatment LINAC, where both components were rotated to test for collisions. To test collision detection accuracy an end-to-end cranial test was performed. The buffer sized required during the registration process to achieve a sensitivity of one was determined via a registration accuracy test. Incorporating the patient-specific CZs, non-coplanar treatment plans were created and compared to clinical coplanar plans for SBRT lung patients (N = 8). A statistically significant change in the mean dose to the lungs was found. Our study indicated that determining patient-specific CZs can be accomplished enabling safe non-coplanar treatment plans.

## List of Abbreviations and Symbols Used

| | |
|---|---|
| 3D | Three-dimensional |
| $\pi$ | Pi |
| AAA | Anisotropic Analytic Algorithm |
| AAPM | American Association of Physicists in Medicine |
| CI | Conformity Index |
| CT | Computed Tomography |
| DICOM | Digital Imaging and Communications in Medicine |
| FN | False Negative |
| FP | False Positive |
| FPR | False Positive Ratio |
| ICP | Iterative Closest Point |
| IR | Infra-red |
| LINACs | Linear Accelerators |
| MLC | Multi-Leaf Collimator |
| MV | Megavoltage |
| OAR | Organs at Risk |
| OBB | Oriented Bounding Box |
| PDD | Percentage Depth Dose |
| PRO | Progressive Resolution Optimizer |
| PTV | Planning Target Volume |
| RF | Radiofrequency |
| RMSE | Root Mean Square Error |
| SAT | Separating Axis Theorem |
| SBRT | Stereotactic Body Radiation Therapy |
| SLD | Sub-lethal Damage |
| SRS | Stereotactic Radiation Surgery |
| SRT | Stereotactic Radiation Therapy |
| TN | True Negative |
| TP | True Positive |
| TPR | True Positive Ratio |
| VMAT | Volumeteric Modulated Arc Therapy |

## Acknowledgements

I would like to express my deep appreciation and gratitude to Dr. Christopher Thomas for his guidance, wisdom and leadership. Your compassion and humour shine as brightly as your intellect. Thank you for your unwavering support, your unerring belief in your students allows us to move mountains.

I would like to thank Dr. Alasdair Syme for being a fount of new ideas.

To the $4\pi$ team, this wouldn't have been possible without being able to wheel my way over to your desks anytime to ask a question or discuss an idea. I would like to thank Brian Little for his essential contributions and expertise, which made this thesis possible. I was very fortunate to have John Lincoln as my Masters-mentor. Thank you for your patience, kindness and brilliance.

To all the staff in the Medical Physics Research and Development AIF lab, I want to say thank you for all your support and friendship throughout this work. In particular this thesis could not have been completed with Kathryn Moran and her invaluable clinical experience.

To Pepper, your support was essential, this was for you. To my family, thank you for always believing in me.

And lastly, to the moon and back, thank you Noah.

# Chapter 1

# Introduction

## 1.1 Preface

More Canadians are diagnosed with lung and bronchus cancers than both breast and prostate combined [1]. Lung and bronchus cancers have notably low five-year survival rates (17%) and kill more people than any other cancer [1]. Approximately 50% of lung cancer patients will be treated with external beam radiation therapy [2]. The goal of the research is to aid in the enabling of $4\pi$ treatment trajectory delivery for extra-cranial sites with the larger aim of improving the quality of the plan. This thesis presents a system that determines patient-specific collision zones to enable safe and deliverable non-coplanar, anatomy-informed, treatment trajectories for patients receiving stereotactic body radiation therapy. Two novel algorithms have been developed to determine patient-specific collision zones which ensure the deliverability of the treatment plans. Resulting treatment plans of the $4\pi$ technique with patient-specific collision zones for SBRT lung were compared to the clinically standard for SBRT lung. This research is intended to directly improve radiation therapy for patients with lung and bronchus cancers.

## 1.2 External Beam Radiation Therapy

### 1.2.1 Medical Linear Accelerator

External beam radiation therapy is most often delivered with medical linear accelerators (LINACs). LINACs generate electrons with an electron gun which then enter an evacuated waveguide where they are accelerated to mega-electron volt (MeV) kinetic energies. These electrons bombard a target, with a high atomic number, to generate MV photons. The LINAC offers high energy photon beams resulting in excellent skin sparing and tissue penetration, along with high dose rates [3].

The five major components which make up a LINAC are: the gantry, the gantry stand, the modular cabinet, the patient support assembly (treatment couch), and the control console [3]. The collimator, which is a part of the gantry head, rotates and collimates the radiation beam as it exits the gantry head. During treatment, patients lie on the treatment couch, which can rotate, while the gantry rotates about them. There are thus three axes of rotation which are displayed in Figure 1.1, and all of these axes meet at a fixed point in space: the isocenter. The couch rotates around a vertical axis, he gantry around a horizontal axis, and the collimator also rotates on an axis that intersects at the isocenter. In fact the isocenter is not a singular point but actually a sphere of 1-2 mm diameter [4] because of mechanical limitations in the movement of the LINAC. A patient is aligned such that the centre of their tumour is aligned to the isocenter, thus as the LINAC components rotate, the tumour remains at the isocenter.

The components which form the treatment beam (Figure 1.2) of the LINAC are the:

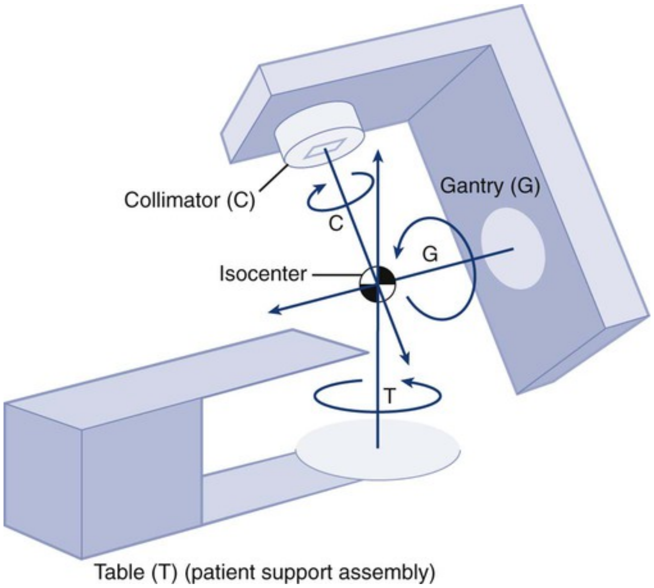

Figure 1.1: Schematic showing the rotation axes of the LINAC [5].

- Injection system,
- Accelerating waveguide,
- Radio frequency power generation system,
- Auxiliary system,
- Beam transport system,
- Beam collimation and beam monitoring system [3].

Electrons are generated via thermionic emission at a heated filament cathode and are then focused into a pencil beam by focusing electrodes. The grounded anode is perforated and the electrons accelerate towards and through it, from the electron gun, into the accelerating waveguide [3].

The accelerating waveguide is an evacuated cylindrical chamber that is subdivided by a series of disks positioned down the chamber. These carefully engineered

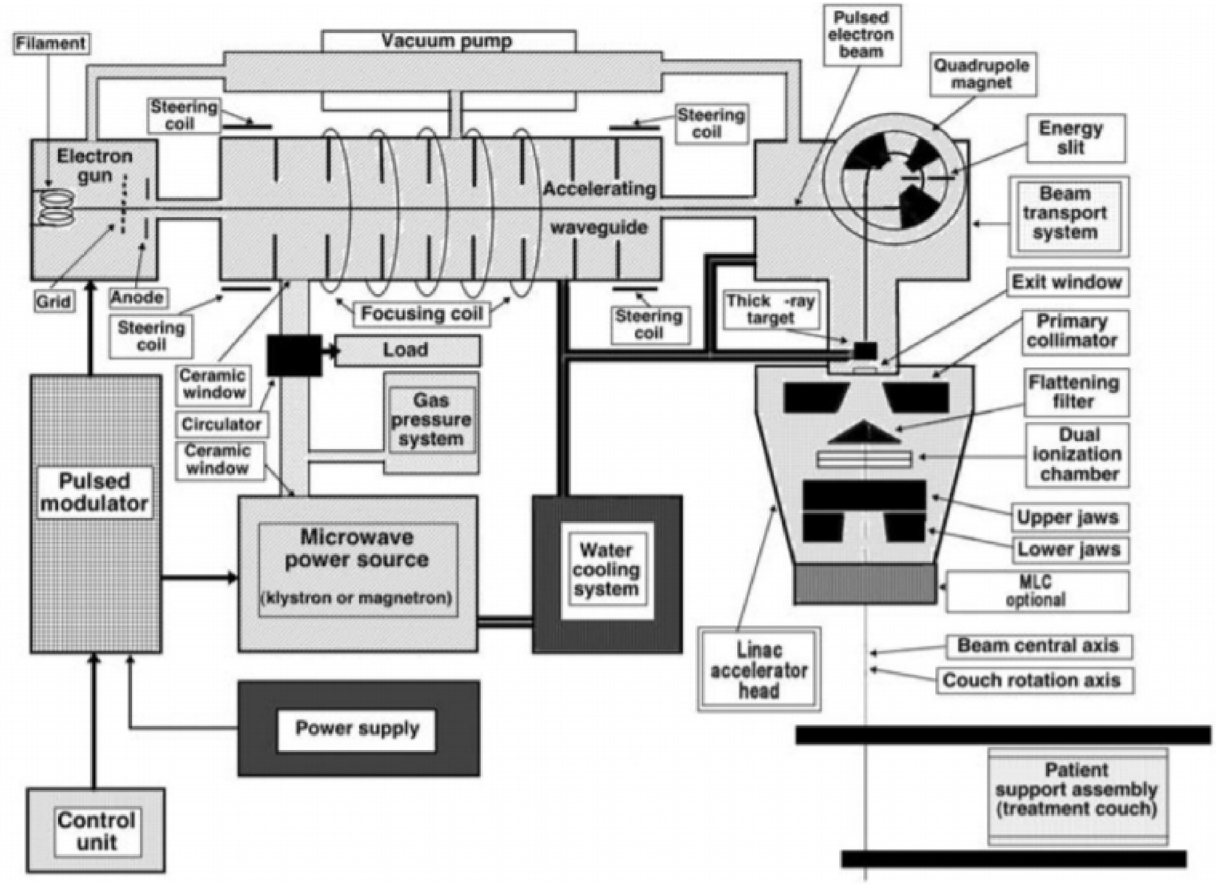

Figure 1.2: Schematic diagram of a LINAC [3].

cavities maintain a radiofrequency (RF) field which creates the electric field required to accelerate the electrons. Steering and focusing coils are used to steer the electrons down the accelerating waveguide [3].

A radiofrequency (RF) power generating system generates the high power microwave radiation used to accelerate the electrons in the waveguide. The RF power generating system is composed of two components: a RF power source and a pulse modulator. Either of combination of a RF driver and a lystron or a magnetron is used to generate and amplify the RF energy. The pulse modulator produces the “high voltage, high current, short duration” pulses required both by the RF power source and the electron injection system to operate. A gas filled waveguide is used to transmit the RF energy from the power source to the accelerating waveguide [3].

Maintaining the beam generating components and the operation of the LINAC, requires several auxiliary systems. These systems are: the vacuum pump system, the water cooling system, the air pressures system, and the radiation leakage shielding. The vacuum pump system maintains the evacuated portions of the LINAC. To transport heat away from various components, the water cooling system circulates water throughout the LINAC. The air pressure system is responsible for moving various beam creation components in and out of the beams path. Finally, the radiation leakage shielding in the gantry head to prevent stray photons from leaking into the treatment room [3].

The Varian TrueBeam STx (Varian Medical Systems, Inc., Palo Alto) LINACs, used at the QEII Cancer Centre, require the bending, or transport, of the electron beam 90° from the exit of the waveguide towards the target or a scattering foil. A 270° bending magnet steers the beam towards the target; this system is still within the vacuum. The electron beam then passes through the exit window into the treatment head [3].

Within the LINAC treatment head are the beam collimation and beam monitoring system. The key components are:

- Retractable x-ray targets,
- Flattening filter and electron scattering foils,
- Primary and secondary collimators,
- Dual transmission ionization chambers,
- Multi-leaf collimators [3].

To produce a 6 MV photon beam, the electrons are accelerated to 6 MeV within the waveguide, travel around the bending magnets, and then impinge on the energy-specific tungsten x-ray target where a small percentage of the electrons are converted to photons and the remainder dissipate their energy in the form of heat. Tungsten is used as it has a high melting and a high atomic number and the rate of photon production is proportional to the square of the atomic number [4]. The intensity of the beam will be forward peaked due to the angular distribution of the emitted photons becoming increasing forward peaked with increasing electron energy. For a standard clinical beam, an energy-specific flattening filter is placed within the path of the beam such that the beam profile is uniform across the beam at a depth of 10 cm within the patient. As the beam energy increases, and thus becomes more forward peaked, the filters becoming thicker along the central axis. For high dose radiation therapy, the flattening filter is removed to produce a flattening filter free beam. For an electron beam, the x-ray target and the flattening filters are removed and instead a scattering foil is placed within the path of the pencil beam [3].

Primary collimation shapes the beam into a circular beam that is fixed in size. Two sets of adjustable jaws create a rectangular field during secondary collimation, with a maximum field size of 40 x 40 $cm^2$ at the isocenter. The final collimation occurs at the multi-leaf collimators (MLCs). This device contains individual, computer controlled, motorized leaves that produce irregularly shaped fields as seen in Figure 1.3. The projected width of the leaves at the isoplane is 2.5 mm for the inner set of leaves and 5 mm for the outer leaves for the Varian TrueBeam STx [6]. The leaves are made of tungsten and designed such that radiation leakage from between the leaves is $3 - 5\%$ of the dose at the isocentre and the radiation through the leaves is less than 2% [3].

For the purpose of patient safety and monitoring the dose delivered to the patient, accurate dose measurement is a must. Dual ionization chambers, which are completely independent from each other, monitor the dose, radial and transverse flatness, symmetry, and the energy of the beam. Once the measured amount of delivered dose matches the treatment plan, the beam is terminated [3].

Several generations of LINACs have passed since their clinical introduction in the 1950's, becoming increasingly sophisticated with every generation. The initial LINACs could not generate electron beams due to their fixed flattening filter. The introduction of a rotating carousel holding the targets enabled the addition of scattering foils and thus electron beams became available. Next independent collimator jaws allowed asymmetric rectangular treatment fields. Introduced in the 1980's, MLCs can shape the beam to match the projection of the target in the beams-eye view (BEV) [7] and enabled the development of intensity-modulated

Figure 1.3: An image of a multileaf collimator system [9].

therapies. Intensity-modulated radiation therapy (IMRT) uses stationary gantry positioning and dynamic MLC movement to deliver small beamlets of varying intensity that when summed produce the desired dose distribution. Advancing from fixed gantry positions to treatment arcs, volumetric modulated arc therapy (VMAT) uses constantly changing beam shapes during treatment delivery in a continuous arc to produce the desired dose distribution. By delivering treatment over a continuous arc, delivery time is reduced while maintaining or improving upon IMRT dose distributions [8].

## 1.3 History of Stereotactic Radiosurgery

### 1.3.1 Principles

Stereotactic radiosurgery (SRS) is a form of radiation therapy where a single, large dose of radiation is delivered to a lesion in the brain or spine via multiple small beams. The defining characteristics of SRS are:

1. High doses ($> 10$ Gy) is delivered in a single, or very few, fractions.
2. Higher delivery accuracy than conventional radiation therapy. SRS can be delivered with sub-millimetre precision [10].
3. Higher dose conformity to the lesion than conventional radiotherapy.
4. More rapid isotropic dose fall-off outside of the lesion than conventional radiotherapy.

The higher delivery accuracy is achieved using image guidance and stereotactic apparatus to immobilize the patient. The high dose conformity is achieved using high-definition MLCs to create small beamlets which highly conform to the lesions. Rapid isotropic dose fall-off is achieved by treating the lesion from many different directions.

### 1.3.2 Stereotactic Brain Surgery

Stereotactic radiosurgery began with stereotactic brain surgery. A stereotactic atlas would be affixed to the patient's cranium to provide a polar coordinate framework for surgeons to aid in localization of surgical targets [11]. The initial head frame can be seen along with Lars Leksell in Figure 1.4. Leksell adapted this technique for radiosurgery with a low energy x-ray source in 1951 [12]. Leksell's work culminated with the invention of the Gamma Knife.

### 1.3.3 Gamma Knife

The Gamma Knife utilizes 179 cobalt-60 sources which are individually collimated and arranged on a hemisphere [14]. The first system available outside of Sweden

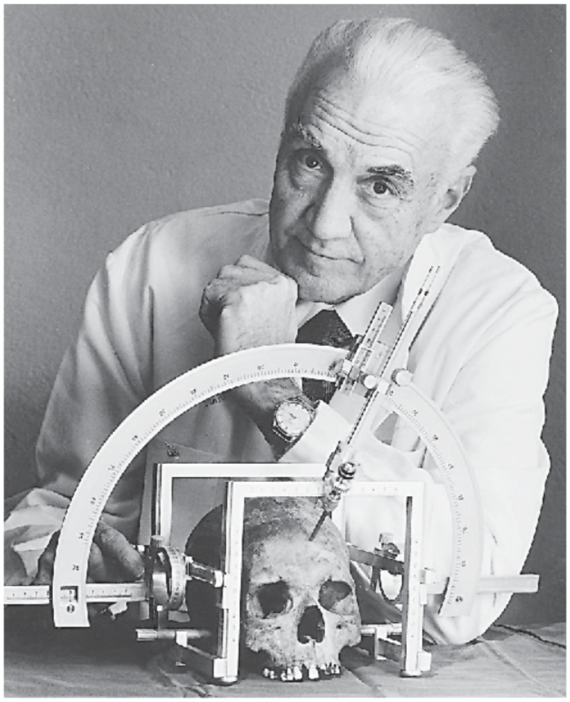

Figure 1.4: Lars Leksell and the stereotactic atlas [13].

was the Elekta Model U [15]. The model U had 201 cobalt-60 sources and utilized a collimator helmet that allowed the individual collimation of each source [16]. A photo of the model U Gamma Knife is presented in Figure 1.5. Elekta continues to produce the Gamma Knife with the most recent iteration being the Leskell Gamma Knife™Icon®.

### 1.3.4 Linac Based C-Arm

SRS returned to its x-ray roots in 1983 with a LINAC-based radiosurgery system [18]. But it was the LINAC-based system developed by Winston and Lutz which established the standard from which the technique grew [19, 20]. Their initial system utilized a stereotactic head frame to immobilize and localize the patient's head and tertiary collimation, as seen in Figure 1.6. This stereotactic frame was fixed to the patient's skull using invasive pins. For both the purpose of patient

Figure 1.5: A patient wearing the collimator helmet being placed within a model U Gamma Knife [17].

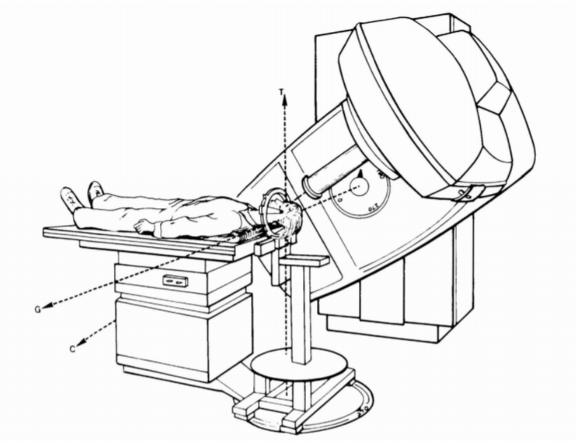

Figure 1.6: Linear accelerator system devised by Winston and Lutz to administer SRS [19].

comfort, and the impracticality of using the frames for multi-fraction stereotactic radiotherapy, frame-less immobilization devices were developed. Because frame-less immobilization is less rigid the frame-based immobilization, image-guidance is required to maintain appropriate target localization in a modern c-arm systems.

### 1.3.5 Cyberknife

The developers of the Cyberknife® focused on using image guidance to ensure accurate dose delivery [21]. A single energy, flattening filter free LINAC is mounted

Figure 1.7: Image of the Cyberknife system [24].

on a robotic arm with six-degrees of freedom and intra-fractional imaging is used to maintain submillimeter accuracy. The intra-fractional images are acquired using two orthogonal x-rays mounted on the ceiling and the resulting images are referenced against digitally reconstructed radiographs (DRR). The intra-fractional imaging informs the adjustment of the robotic manipulator that adjusts the positioning of the LINAC, retargeting the radiation beam [22]. These components can be seen on Figure 1.7. Cyberknife preforms non-coplanar treatments, but it is important to note that the Cyberknife delivers radiation using the "point-and-shoot" technique, this is to allow for the intra-fractional imaging. Thus, non-coplanar arc treatments are currently non-viable, although an active area of research [23].

## 1.4 Stereotactic Body Radiation Therapy

### 1.4.1 Principles

Stereotactic body radiation therapy (SBRT), also referred to as stereotactic ablative body radiation therapy (SABR), applies the same principles as SRS but to extra-cranial sites. Primarily lung, liver, and spinal tumours are treated using

SBRT [25]. A unique challenge associated with SBRT is motion due to respiration, cardiac function, peristaltic activity, and organ filling and emptying [25]. Motion management begins at the simulation stage when patient-specific tumour motion is determined. This informs the required motion management. Motion management can take the form of body frames, image guidance, optical tracking, and respiratory gating [25]. Localization of the tumour is best achieved using image guidance combined with robotic six-dimension motion enabled couches that can address both translation and rotation errors in alignment.

### 1.4.2 C-Arm LINAC

The first clinical application of stereotactic radiotherapy to an extra-cranial target was performed by Hamilton *et al.*, who utilized a spinal stereotactic frame to treat paraspinal neoplasms [26]. The frame utilised skeletal fixation and enabled the delivery of a single fraction treatment of a median dose of 10 Gy [26]. The same year, Blomgren *et al.* applied stereotactic principles to lung, liver, and retroperitoneal space using a frame placed over the patient and a vacuum cushion [27]. The current standard for C-arm LINAC SBRT is that "image-guided localization techniques should be used to guarantee the spatial accuracy of the delivered dose" and for "all SBRT patients with targets in the thorax or abdomen, a patient-specific tumour-motion assessment is recommended" [25].

### 1.4.3 Cyberknife

Cyberknife is well-suited to SBRT delivery, due to its frame-less localization techniques. It was initially trialed for lung tumours with implanted fiducial markers being used to track the tumour's location [28]. The current methods for SBRT

Figure 1.8: Vest used to track patient respiratory motion [30].

localization are bony structure tracking of the spine, comparison to DRRs, implanted fiducial marker tracking, and soft tissue tracking [29]. The soft tissue tracking makes use of the density difference between the target and the surrounding lung tissue. To track respiratory motion, the Cyberknife system uses motion at the skin as a surrogate for internal motion [29]. Visible light sources are placed on the patient's abdomen to track the respiratory motion (see Figure 1.8) which assists the Cyberknife in correlating breath and tumour movement.

### 1.4.4 Vero

Developed by BrainLab (BrainLab AG, Feldkirchen,Germany) and MHI (Mitsubishi Heavy Industries, Tokyo, Japan), Vero is a dedicated SBRT treatment platform, with the most notable feature being the gimbaled treatment head. A

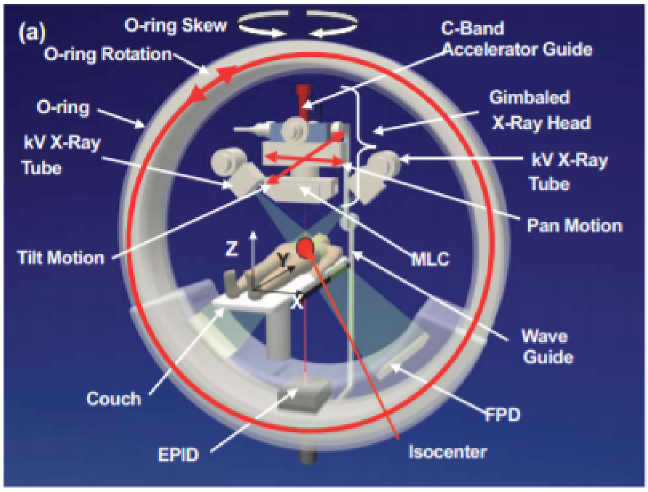

Figure 1.9: Diagram of the Vero system [31].

system concept diagram can be seen in Figure 1.9. The treatment head is mounted on two gimbals, allowing it to both tilt and pan rotate [31]. As with Cyberknife, Vero offers "real-time tumour tracking" via orthogonal x-ray imaging. The pan and tilt rotations "provides quick pursuit beam motion around the isocenter" to compensate for organ motion [31]. The orthogonal x-rays also allow the six-degrees of freedom couch to ensure proper localisation of the target. The couch does not rotate, instead the O-ring, on which the imaging and treatment systems are mounted, skews. Simultaneous rotation and skewing of the O-ring enables non-coplanar arc delivery, referred to as dynamic wave arc (DWA) [32].

## 1.5 Radiobiology

### 1.5.1 Standard Fractionation

Fractionated radiation therapy subdivides the treatment into reoccurring treatments whose total dose sum to the prescribed dose. It is the dose limit of side effects to health tissues that limits the dose that can be delivered in a single fraction. Thus by dividing treatments into fraction, more dose can be delivered to the tumour while increasing the dose tolerance of health tissues because by providing time for repair of sub-lethal damage. There are four key radiobiology concepts, the four Rs of Radiobiology, which guide the practice of fractionation:

- Repair: cells repair sub-lethal damage (SLD) between treatment fractions which increases cell survival.
- Repopulation: cell division occurs in between treatment fractions resulting in increased cell survival.
- Reassortment: cells have varying radio-sensitivity dependent on which stage of the cell cycle they occupy. The time between treatment fractions allows for cells in radio-resistant stages to enter radio-sensitive stages and thus increases cell death in the subsequent treatment.
- Reoxygenation: hypoxic cells become oxygenated in between treatment fractions and thus more radio-sensitive leading to increased cell death [33].

Repair and repopulation increase tumour cell survival, while reassortment and reoxygenation increase tumour cell death. Healthy tissue benefits from repair and repopulation reducing undesirable side effects.

Standard fractionation regimes are modelled using the linear-quadratic model, which assumes there are two modes of cell damage which could lead to cell death. The first mode is related to a single, possibly lethal, event which increase linearly with dose. The second mode is due to multiple sub-lethal events compounding to potential kill a cell, which increase quadratically with dose [33]. The fraction of cells which survive ($S$) a dose ($D$) is expressed in Equation 1.1.

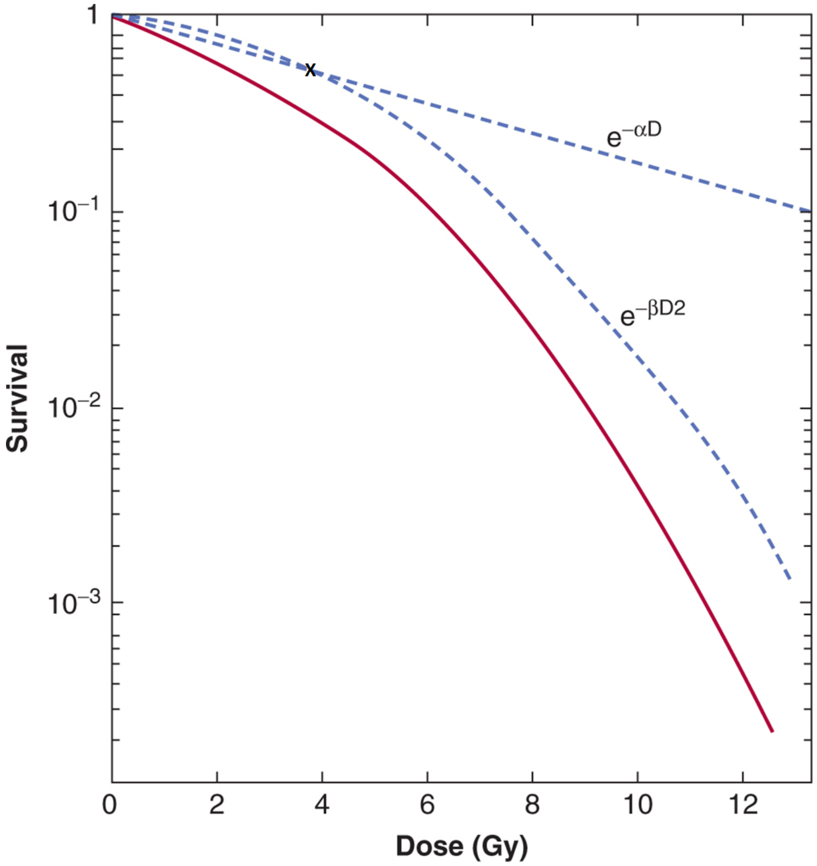

Figure 1.10: Survival curves and parameters in the Linear Quadratic model. The overall cell survival curve (solid lines) is plotted with each component in the LQ equations as the linear components and quadratic components (dotted lines). The dose marked by an X, is point when the dose is equal to $\frac{\alpha}{\beta}$ [34].

$$S = e^{-\alpha D - \beta D^2} \tag{1.1}$$

The variables $\alpha$ and $\beta$ are constants which describe the linear and quadratic components of survival [33]. These two constants vary from organ to organ. The individual components are plotted in Figure 1.10, where it can be seen at the point $D = \frac{\alpha}{\beta}$ the cell death due to the two components becomes equal. Cell death being defined as a loss of reproductive capabilities.

Because $\alpha$ and $\beta$ vary from organ to organ, $\frac{\alpha}{\beta}$ is unique to each tissue. For example, tissues which are radioresistant, or “late responding”, have a lower $\frac{\alpha}{\beta}$ fraction, which would mean the quadratic components dominates. Whereas more radiosensitive tissues, “early responding”, have a higher $\frac{\alpha}{\beta}$ value, thus the linear component is more dominant [35].

### 1.5.2 Stereotactic Radiosurgery Fractionation

When the radiobiological principles which guide traditional fractionation are applied to stereotactic radiosurgery we find:

- Repair: stereotactic treatment deliveries can be lengthy, providing time for SLD repair during treatment.
- Repopulation: due to the overall shorter treatment time, due to only delivering a single fraction, repopulation plays no role.
- Reassortment: due to the overall shorter treatment time, due to only delivering a single fraction, reassortment plays no role.
- Reoxygenation: single fraction treatments cannot exploit reoxygenation [35].

While SRS does not exploit the 4 Rs of Radiobiology, clinical results have shown it can effectively achieve sufficient tumour control [35].

Although SRS does not provide time for reassortment and reoxygenation, the high dose, 10 Gy and above, not only uses DNA damage to achieve cell death but also damage to vascular endothelial cells. Microvascular dysfunction acutely disrupts tumour perfusion and leads indirectly to cell death [35]. Because the linear-quadratic model was created using experimental data determined with dose values below those used in SRS, the model’s applicability comes into question.

Evidence has suggested that microvascular damage plays a role in cell death and is not accounted for in the model [35].

In place of repopulation and repair, tissue sparing is achieved via the rapid dose fall-off outside the target volume achieved by the removal of the flattening-filter, high definition MLCs, and using many treatment angles. But the size of target which can be treated using SRS is limited, as a small target means a small volume of tissue around it receiving a high dose [35]. As the target increases in size, the dose to the surround healthy tissue will also increase thus, for slightly larger targets, fractionated stereotactic radiotherapy is a better option.

### 1.5.3 Single vs. Multi-fraction Stereotactic Radiotherapy

Single fraction SRS is ideal for small targets which do not abut sensitive organs. Intermediate sized targets, or those near sensitive structures, are better suited to stereotactic radiation therapy (SRT) [36]. SRT is delivered in the same manner as SRS, but the treatment is split into three to five fractions due to the larger dose spill over from the target volume.

The benefit of SRT compared to SRS is that it expands the therapeutic window. The therapeutic window is the ratio between the probability of tumour cure and the probability of complications [35]. Fractionating the treatment allows time for repair and repopulation in a sensitive organ and reduces the dose received per treatment. Additionally, reoxygenation of cells deeper within a larger tumour between treatments will lead to greater cell death. Also note, SBRT can be delivered in a single to few fractions, depending on the location and size of the tumour [37].

## 1.6 Clinical Radiation Therapy

### 1.6.1 Clinical Cranial Stereotactic Radiation Therapy

For SRS and SRT, the standard clinical arc arrangement is one coplanar 360° arc and three non-coplanar 180° arcs with the couch rotated to 90°, 45°, and 315°. The planning target volume (PTV) includes the gross volume of the tumour in addition to a margin (2 mm) which accounts for microscopic disease, set-up uncertainties, machine tolerances, and intra-treatment variation [4]. When the brainstem, chiasm, optical nerves, and the optical tracts are contoured an additional 2 mm margin is added. Other OARs that will be contoured are the eyes and the lens. Prescription dose for PTVs is dependent on the volume of the PTV as recommended by RTOG 9508 [38].

### 1.6.2 Clinical Extra-Cranial Stereotactic Radiation Therapy

There are generally two doses prescribed for lung SBRT at the QEII Cancer Centre: either 48 Gy in 4 fractions or 60 Gy in 8 fractions. The PTV, similarly to as described in 1.6.1, also accounts for internal movement due to respiration in extra-cranial SBRT. The standard arc template is two partial gantry arcs, 190° each, ranging from 180° to 10° past 0° (see Figure 2.21) with the collimator angles at complementary 30° angles. The spinal cord, trachea and esophagus are contoured on the patient's CT scan with an additional 5 mm margin to create a planning organ at risk volume. Both lungs, the heart, the bronchus, the chest wall, and the aorta are contoured. When the treatment planning is being optimized there are several optimization goals which are outlined in Table 1.1 for the 48 Gy in 4 fractions prescription, these values are informed by RTOG 0915 [39].

| Volumes | Requirement |
|---|---|
| PTV | |
| Volume receiving 90% of the prescribed dose | Should be $> 99\%$ of the PTV volume |
| Conformity Index | Should be $< 1.2$ at prescription isodose level |
| Maximum dose to the volume | Should be approximately 100% |
| Lungs | |
| Volume receiving 20 Gy | ideally $\leq 10\%$ |
| Mean dose to the volume | Should be $< 6$ Gy |
| Trachea | |
| Maximum dose to the volume | $< 34.8$ Gy |
| Esophagus | |
| Volume receiving 18.8 Gy | $< 5$ cc |
| Maximum dose to the volume | $< 30$ Gy |
| Bronchus | |
| Volume receiving 15.6 Gy | $< 4$ cc |
| Maximum dose to the volume | $< 34.8$ Gy |
| Heart | |
| Volume receiving 28 Gy | $< 15$ cc |
| Maximum dose to the volume | $< 34$ Gy |
| Spinal Cord | |
| Volume receiving 28 Gy | $< 0.35$ cc |
| Volume receiving 28 Gy | $< 1.2$ cc |
| Maximum dose to the volume | $< 26$ Gy |

Table 1.1: A portion of the dose guidelines used at the QEII Cancer Centre for lung SBRT treatment plans. The prescribed dose is 48 Gy. Conformity index is the volume receiving 90% of the prescribed dose divided by the total volume of the PTV.

## 1.7 $4\pi$ Radiation Therapy

### 1.7.1 Origins of $4\pi$

Referring to the solid angle of a complete sphere, $4\pi$ radiation therapy examines every viable treatment angle in the sphere formed by the 360° of rotation of the gantry and the 180° of rotation of the couch. Seeking to reduce the dose to organs at risk (OARs) Yang *et al.*, developed a method to determine optimized trajectory-based non-coplanar sub arcs for VMAT [40]. The couch-gantry trajectories are determined by first calculating the geometric overlap of the PTV and OARs at each treatment angle as seen from the beams-eye-view. These values are displayed in a geometric overlap map, and choosing trajectories which minimizes the overlap score creates an ideal treatment path [40]. At Dalhousie University, this was expanded upon by MacDonald and Thomas [41]. They ensured that the treatment arcs would be clinically deliverable and matched the technical limitations of current LINAC technology and the Eclipse Treatment Planning System (Varian Medical Systems Inc., Palo Alto, California, United States), as well as modifying the algorithm to take into account foreground versus background location of the OARs with respect to the PTV and the radio-sensitivity of the OARs. Using the optimization algorithm for cranial RT, MacDonald *et al.* achieved a 19% decrease to mean dose to the OARs and a 14% reduction of the maximum dose [42]. Of note, both MacDonald and Yang's work focused on cranial targets. This algorithm had to also navigate around collision zones, which are combinations of couch and gantry coordinates which may result in a collision between the gantry and couch or patient. Yang *et al.* initially blocked out two quadrants of the overlap map as collision zones. MacDonald *et al.* manually measured cranial collision zones using a Varian TrueBeam STx linear accelerator and a cranial anthropomorphic phantom with a 5 cm buffer used to account for variety in patient set-up [41]. The collision zones constructed by Macdonald *et al.* reduced the amount of $4\pi$ space occupied by the collision zones, thereby providing more degrees of freedom for trajectory optimization.

### 1.7.2 Current Work from Other Groups

Dynamic non-coplanar stereotactic radiation therapy is a very active area of research with several recent cranial $4\pi$ publications [43–52]. Progress on extra-cranial $4\pi$ has been more limited, most likely due to the struggles with collision zone identification.

Liang *et al.* [53] investigated non-isocenteric trajectory modulated arc therapy for accelerated-partial breast irradiation. Couch rotation and translation are combined to reduce dose to the total breast volume when patients are being treated in a prone position. While OARs are not considered during the trajectory selection, the primary purpose was to reduce dose to the healthy breast tissue. Because the patient is treated prone, and gravity is pulling the breast away from the chest, OARs are removed from the beam path and need not be considered. Dong *et al.* [48] examined $4\pi$ non-coplanar liver SBRT. They compared clinical treatment plans, composed of two full arcs, to their $4\pi$ treatment plan made of 14 to 22 non-coplanar static IMPRT fields. They found superior results in tumour coverage, normal liver tissue sparing, and critical organ sparing with their technique. Woods *et al.* [54] expanded on Dong *et al.*'s [48] work and compared clinical coplanar VMAT, non-coplanar VMAT, and the static $4\pi$ technique, and determined the non-coplanar VMAT is not a viable replacement for static $4\pi$ liver SBRT when examining dose spillage and the dose to OARs. While the $4\pi$ treatment delivery time was significantly longer (45 minutes), due to the manual couch rotation requiring therapists to entire and exit the treatment room, the authors claim that should automated delivery become feasible the treatment time would then match non-coplanar VMAT delivery time.

Ng *et al.* [55] examined coplanar and non-coplanar VMAT and IMRT SBRT for lung patients. They found the that the lung volume receiving greater than 20 Gy can be reduced using non-coplanar treatment methods, but no other benefits were seen when comparing non-coplanar IMRT and non-coplanar VMAT. Dong *et al.* [56] examined lung SBRT comparing co-planar IMRT to non-coplanar IMRT, which they refer to as static $4\pi$. They found significant improvement in dose to OARs and sparing of the normal lung when static $4\pi$ was used. Again, the issue of treatment time is raised, as well as collision zones. The group posited that newer generations of C-arm LINACs will eliminate the treatment time issue, while acknowledging that delivery sequence optimization and collision avoidance must be addressed prior to clinical implementation.

Langhan *et al.* [51] introduce what they called Noncoplanar VMAT Optimization (NOVO), which determines a non-coplanar arc solution by examining every possible beam solution in the $4\pi$ space and then determining a dynamic path between them. For a lung and a liver case, the dose to OARs from static $4\pi$ (non-coplanar IMRT), non-coplanar VMAT, and NOVO treatment plans were examined. While the static $4\pi$ treatment plan produced the best results, the dynamic NOVO plan came closest in dosimeteric results to that achieved by static $4\pi$. NOVO would still face the same challenge that most techniques face, which would be the mechanical limitations of the modern LINAC.

## 1.8 Motivation

It has been well documented that $4\pi$ delivery reduces dose to OARs for cranial cases [41, 44, 46, 52] and has shown promising results in applications for extra-cranial sites [48, 53, 54, 56]. But a major barrier to the clinical application of the $4\pi$ treatment technique to SBRT is the unknown characteristics of the collision zones. Extra-cranial sites vary greatly in the physical location of the PTV and the positions that the patient adopt for treatment. During lung radiotherapy, a patient must place their hands above their head, resting on the treatment bed, to avoid irradiation of the arms. But due to variation in patient mobility, the patient's arms can rest in several different positions. The arms, torso, head, and legs could potentially collide with the treatment head. If a collision occurs with a patient on the treatment bed, it could result in injury or rescheduling and replanning of the patient's treatment and may reduce the patient's confidence.

Because of the increased amount of patient volume within the $4\pi$ sphere, it is clear that the collision zones for extra-cranial patients will be larger than those for cranial. This would result in smaller amount of feasible couch-gantry space. Additionally, the variation in PTV locations is much greater for extra-cranial patients as the total volume of the brain is significantly less than the lungs. This will result in great variance in the shape of the collision zones as well. Thus it is essential to determine *patient-specific* collision zones.

## 1.9 Previous Work in Collision Detection

The earliest work in collision detection focused on developing tools to aid treatment planners by displaying graphic simulations of the couch and gantry in treatment

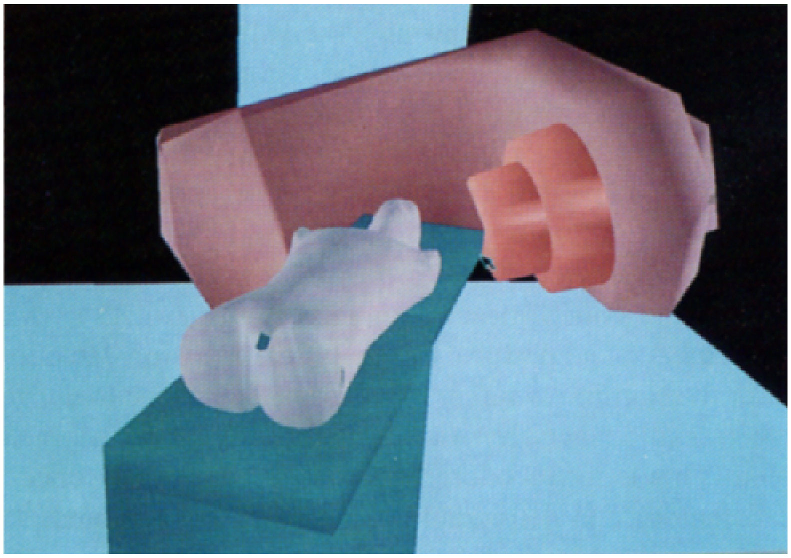

Figure 1.11: A rendering of the patient, gantry, and couch in treatment position which would have been displayed to the planners [58].

position and indicating to the planner if a collision would occur at that angle. While Kesseler *et al.* [57] did not consider the volume occupied by a patient, Humm *et al.* [58] did. Using a model of the Rando Phantom, as seen in Figure 1.11, they became the first group to consider modelling patient-gantry collisions.

With increased computational power, research into collision zones has expanded. Still, some groups choose to only calculate couch and gantry collision zones [59, 60]. Others choose to only use a single surface scanned patient contour to act as a surrogate for all patients [48, 56, 61–63], although many of these groups are more focused on delivery technique [48, 56, 62]. A small number of outliers have chosen to move away from the computational approach. Papers which focused on overlap map navigation used phantoms as patient stand-ins and manually measured on a LINAC the colliding gantry and couch combinations [40, 41, 64]. Other groups have determined tables and graphs of permissible angle combination by manually measuring cranial collision zones with a Rando phantom [65] or a stereotactic body frame [66] on the treatment bed.

With the increased prevalence of non-coplanar arc, patient-specific collision detection has become increasingly valued. Most commonly patient contours are acquired from CT scans [67–72]. But these scans fail to capture the entirety of a patient's body. One way to overcome this is to register a patient's CT scan to a surface scan of the patient [72] or a phantom [71]. Cardan *et al.* developed a method based solely on surface scanning [68]. By installing three commercially available surface scanners in the simulation room it was possible to simultaneously acquire the CT simulation and a full body patient mesh. Additionally, due to the set-up, the scans were acquired with the knowledge of how the scanner coordinate system relates to the CT scanner coordinates. Four patients were scanned for computation of collision zones and also used to determine a small subset of manually measured collision zones. These computed collision zones were calculated with buffers applied. The study was comprehensive and was found to add only one minute to a patient CT simulation. Cardan *et al.* produced a comprehensive methodology by which to acquire patient-specific collision zones regardless of treatment site [68]. To prevent the clinical burden of set-up and maintenance of this system, our work seeks to expand on the patient contour expansion method. Recently a similar methodology by Islam *et al.* has been published that also takes into account the on-board imaging components and explicitly described how to assure the couch is placed appropriately, as the couch is not captured by the surface scanner [73].

Nioutsikou *et al.* were the first group to consider expanding the patient contour beyond what was captured within the CT simulation [74]. They did this by creating a set of pre-defined extensions based on a RANDO phantom, "one set with the centre of origin in the head and neck region that can be added to a head and neck patient scan, one with the centre of origin in the thorax and one in the

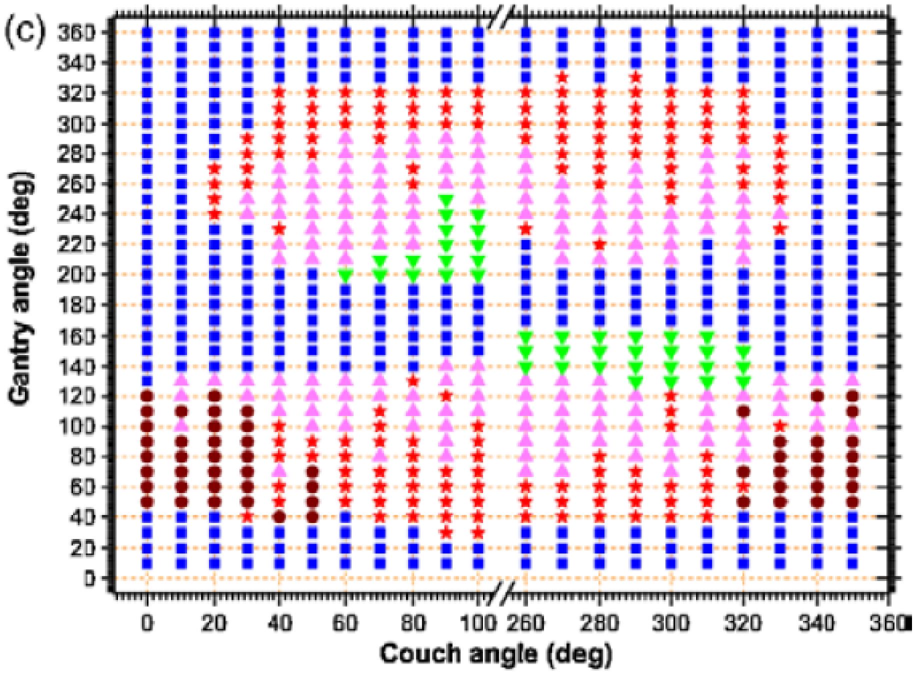

Figure 1.12: Collision zone map for an abdominal case (■: collision-free space, ▲: collision with the couch-top, ▼: collision with the couch-base, ●: collision with the patient's body, ∗: potential collision space) [74].

abdominal region" [74]. Figure 1.12 shows the abdominal collision zone calculated by Nioutsikou's methodology.

The paper which most closely matched the collision detection methodology utilized in our work was Mann *et al.*'s paper [71]. An anthropomorphic phantom contour was registered to a cranial patient's contour, which contains just the head, to account for the volume of the patient outside the CT scan. This method closely mimics our own, but diverges in the final collision detection step. Their work is limited to cranial patients, where as we expanded this concept to extra-cranial patients.

## 1.10 Specific Aims

The specific aims of this thesis are two-fold:

1. To increase the amount of usable $4\pi$ space by the creation of patient-specific collision zones by means of an automated method, thereby increasing the clinical utility of $4\pi$ SBRT treatments.
2. To investigate the dosimeteric advantage of $4\pi$ SBRT over coplanar SBRT for lung patients.

Determining patient-specific collision zones can ensure the deliverability of $4\pi$ SBRT treatment plans. The purpose of this research project is to create a system by which to determine these collision zones without additional clinical steps. To do this, an algorithm will be developed to expand CT information gathered during the normal treatment path.

To expand the CT information, a library of full-body patient optical scans was collected. A registration algorithm was developed to combine a patient's CT scan with a best-fit optical scan from the library, along with the treatment couch and immobilization equipment. This completed patient contour was then run through a collision detection algorithm. The result is a patient-specific collision zone. These collision zones were used to inform the determination of $4\pi$ treatment trajectories for SBRT. Those trajectories were then VMAT optimized in the Eclipse Treatment Planning Software. The dose to OARs, conformity, and overlap scores were compared to the clinically delivered plans to assess the benefits of $4\pi$ SBRT. Additionally, the algorithms were assessed for accuracy.

# Chapter 2

# Methods and Materials

The goal of this research project was to create a methodology for determining patient-specific collision zones in order to enable $4\pi$ SBRT treatment planning. The methods described in our work were designed to minimally affect the clinical workflow. This was accomplished by primarily utilizing data collected during the standard treatment planning process and supplementing it with additional data. A library of full-body optical patient scans was acquired to supplement CT data to create artificial body contours, with the intention to prevent future full-body patient scans from needing to be acquired.

## 2.1 Creation of Patient Library

A collection of full body, three dimensional (3D), optical patient scans were obtained from patients receiving SBRT treatment at the QEII Cancer Centre, with approval from the Nova Scotia Health Authority's Research Ethics Board. The scans were obtained using a Creaform Go!SCAN 50 (Creaform Inc., Lévis, Quebec, Canada), shown in Figure 2.1, a handheld surface scanner which uses a combination of white and infrared light to create a 3D polygon mesh of the patient. A 3D polygon mesh is made up of a collection of points connected by vertices and edges. The Go!Scan flashes a pixelated pattern of white light onto the surface which it observes with its two built in cameras. It uses this information to determine spatial

Figure 2.1: Image of a Creaform Go!SCAN 50 which was used to collect patient scans during our study [75].

information about the surface. The infrared camera and small infrared reflective stickers are used to help the camera localize itself in space. Scans were acquired with the patients in treatment position, on the treatment bed with their vacuum cushion and immobilisation equipment in place, with a resolution of 1 cm. Post-processing was completed in VXelements (Creaform Inc., Lévis, Quebec, Canada). Any holes in the mesh were closed, patient facial features where blurred to assure anonymity, and the wing board was removed if it was present. See Figure 2.2 for an example of a processed patient scan. Once the mesh was fully processed it was exported as a point cloud, which are sets of points in 3D space.

The exported point clouds were organized into a library. Each scan was categorized by whether a wingboard (Figure 2.3) was used, the positioning of the patient's arms, and the width and depth of the patient's chest. Example library entries can be seen in Figure 2.4. The wingboard aids patients by providing them a surface to

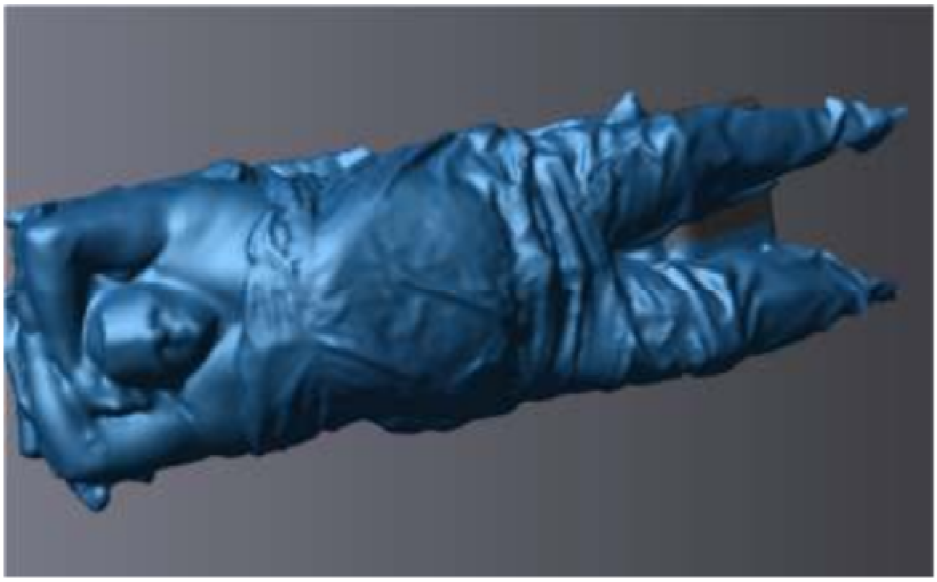

Figure 2.2: An example of a post-processed patient surface scan. Holes in the mesh have been closed, the wingboard has been removed, and the patient's features have been anonymized.

rest their arms on. The arm position categories were "wide" or "narrow" based on the distance between the patient's elbows. Greater than 60 cm between the tips of the elbows is "wide" and less than is "narrow". Initially, we had intended to have more nuanced categories for patient arm positioning but due to the limited library size this was not possible. Patients receiving SBRT undergo a planning CT simulation, which captures both the internal and external anatomy of the patient in evenly spaced transverse slices. The CT simulation was examined in Eclipse treatment planning software to determine the dimensions of the patients' chests. Measurements were taken at the slice containing the centre of mass of the patient's scan as seen in Figure 2.5. The measurements act as a surrogate for the patient's size. In total 11 patient scans were acquired, but one was rejected as the patient could not raise their arms above their head. Initially, we received ethics approval to scan up to 25 patients. This number was selected based on average number of lung SBRT patients per week and the time remaining for the study. Unfortunately, due

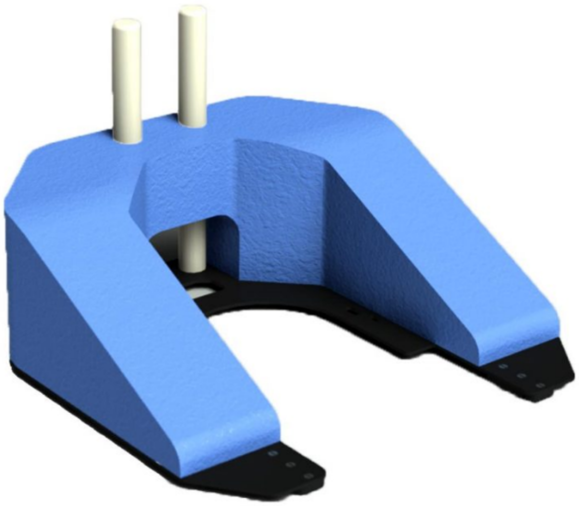

Figure 2.3: Image of a wingboard used for patient positioning and arm support [76].

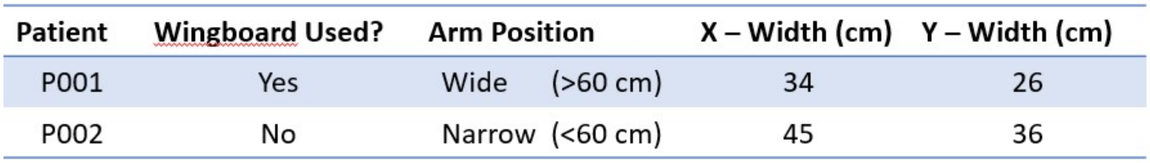

| Patient | Wingboard Used? | Arm Position | X – Width (cm) | Y – Width (cm) |
|---|---|---|---|---|
| P001 | Yes | Wide (>60 cm) | 34 | 26 |
| P002 | No | Narrow (<60 cm) | 45 | 36 |

Figure 2.4: Examples of patient entries into the surface scan library and the elements which categorize them.

to the COVID-19 pandemic, access to the cancer centre was restricted due to increased patient health concerns and in-person data acquisition had to be cancelled. While 11 patients was not the initial goal set forth for this project, it did provide a sufficient test size for initial testing of the methodology.

## 2.2 Importation of Patient Information

The ideal application of this system is the creation of full body contours for patients who have not been surfaced scanned. All SBRT patients receive a treatment planning CT simulation that is contoured as per the clinical standard

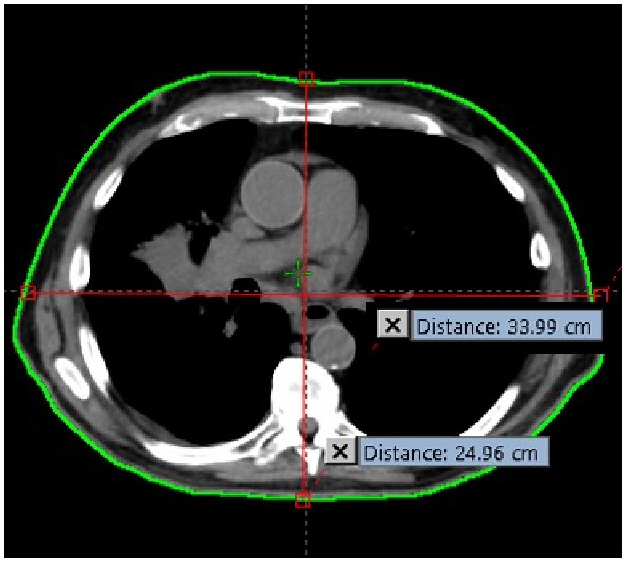

Figure 2.5: An CT slice of a patient with the measurements in the x- and y-dimension measurements.

within our cancer centre. Contouring refers to the process by which a two-dimensional outline is drawn around structures on slices of a CT simulation. These outlines are transformed into a 3D volume by interpolating between the slices. Of the clinical contours, the following were utilized within this research to construct the collision zones: the outer body, couch surface, and PTV contours. Outer body contours encase the entirety of the patient captured within the CT scan. Lung patients are imaged from their temples to their waist.

Two additional structures were contoured: the SBRT immobilization board and the “chin” contour. Part of the immobilization equipment for SBRT treatment is the SBRT board onto which the wing-board docks; it is displayed in Figure 2.6. The SBRT board is used for every patient, and the algorithm used it for alignment of the wing-board. Additionally, a small sphere (1 cm diameter) was contoured within the patient’s chin, as defined by the user. Because the chin contour was only for the purpose of the first initial alignment of the surface scan, it was non-essential for a strict metric for the location of the chin contour.

Figure 2.6: Image of an SBRT immobilization board [76].

Each patient's contour set was exported from Eclipse as a Digital Imaging and Communications in Medicine (DICOM) file and imported into MATLAB (The MathWorks Inc., Natick, Massachusetts, U.S.A.). When DICOM files are exported, the contours are not exported as meshes, but instead as point clouds. For each transverse slice of the CT, a set of 3D dimensional coordinates are provided. When each slices' set of points are combined, a point cloud representing the contour is created.

## 2.3 Full-body Contour Creation

### 2.3.1 Virtual Treatment Room

A virtual treatment room was created within the MATLAB environment. A 3D space was established with the unit space between points representing one millimetre within the physical treatment room. The axes of the room are shown in Figure 2.7 and match with those utilized in Eclipse. The origin of the 3D space is

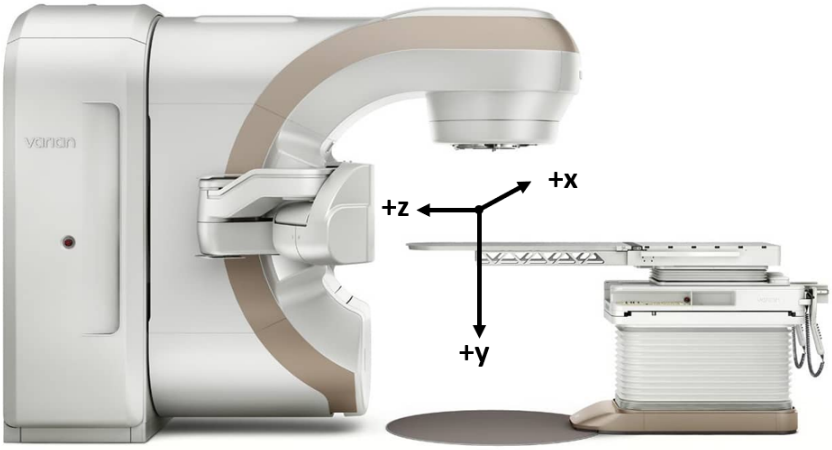

Figure 2.7: The DICOM coordinate system used in the Eclipse and MATLAB enviroment [77].

analogous to isocentre.

Patients are aligned in the treatment room such that the centre of mass of their PTV is at isocentre and this was replicated in the virtual treatment room. After extracting the PTV point cloud from the imported DICOM file, the centre of mass was calculated, and with the use of a translation matrix, all of the CT contours were transposed such that the centre of the PTV and the origin of the virtual treatment room were the same point. The translation matrix, $T_{trans}$ , moves every point in a point cloud by the same distance and is represented in Equation 2.1. The centre of mass of the PTV point cloud, $R$, was used to compute a translation vector for the matrix, $T_{trans}$, where the elements were equal to the negative of $R$.

$$T_{trans} = \begin{bmatrix} 1 & 0 & 0 & 0 \\ 0 & 1 & 0 & 0 \\ 0 & 0 & 1 & 0 \\ -R_x & -R_y & -R_z & 1 \end{bmatrix} \tag{2.1}$$

### 2.3.2 Selection of the Library Scan

Once the patient CT was imported and aligned it had to then be registered to a surface scan from the library. For the testing which occurred in our work, the surface scan which corresponded to the CT of the patient was excluded from the library for the formation of that patient's collision zones. The first step to selecting the appropriate library scan was selecting whether the patient used a wing board and the positioning of the patient's arms. This limited the pool of potential library scans. Next, the centre of mass of the body contour was determined and a slice of the point cloud was taken in the transverse plane at that point. Then the depth and width of the patient was measured along the coronal and saggital axis of that slice. The library scan which most closely matched those dimensions was then selected as the matching scan.

### 2.3.3 Registation of the Scans

The outline for the registration process can be seen in Figure 2.8.

Because, the library scan had the origin, [0,0,0], placed in the chin, when it was imported into the virtual treatment room the library scan was automatically aligned such that the chin was placed at isocentre. The location of the centre of mass of the CT chin contour determined the vector, which formed the translation matrix, that was applied to the library scan. This initially aligned the CT and library scan such that the chins of both models matched.

Because the surface scan was selected based on the width and depth of the patient, the height disparity between the patient and the selected surface scan had to be addressed. The CT point cloud was divided into two portions, the "neck" and

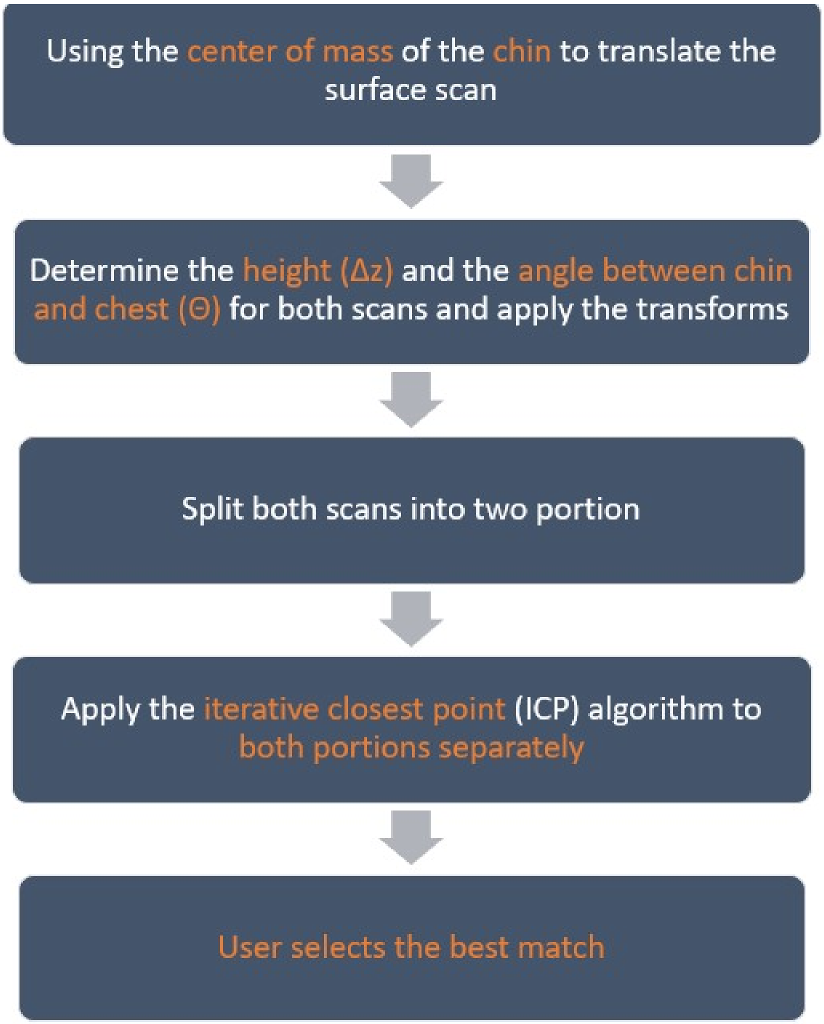

Figure 2.8: Outline of the contour registration process.

"chest" regions by separating the scan at the mean clavicle position for the patient population (see Figure 2.9), and the surface scan was cropped to match those CT portions. The most anterior point of the patient's chin and chest were determined, for both point clouds, by finding the minimum y-values of both portions down the centre line of the scans. The horizontal distance between those points in the z-dimension, Δz, was determined for both the surface scan and the CT scan (see Figure 2.10). A scaling transform was then applied to the surface scan based on the ratio of the two distances. This scaled the surface scan such that the height disparity between the two patients, the surface scanned patient and the CT patient, has been accounted for. The scaling matrix is shown in Equation 2.2.

Next, the two dimensional vector which connects the points used to determine the height disparity along the z-plane was calculated, $v_{z-plane}$. The angle between $v_{z-plane}$ and $\Delta z$, $\theta$, was calculated for each scan (see Figure 2.10). The difference between the angles was used to transform the surface scan by rotating it around the x-axis using the rotation matrix shown in Figure 2.3. This was done because the surface scan was not aligned such that the surface of the treatment couch is parallel to the z-axis, due to the limitation of the scanning software, thus this had to be to accounted for.

$$T_{scaling} = \begin{bmatrix} 0 & 0 & 0 & 0 \\ 0 & 0 & 0 & 0 \\ 0 & 0 & \frac{\Delta z_{CT}}{\Delta z_{SurfaceScan}} & 0 \\ 0 & 0 & 0 & 1 \end{bmatrix} \tag{2.2}$$

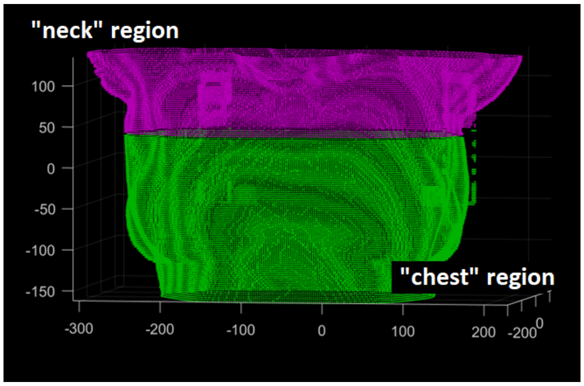

Figure 2.9: An example of a patient CT point cloud split into the "neck", the superior, and "chest", the inferior, region. The scans are split at the mean position of the patient populations' (N=8) clavicle.

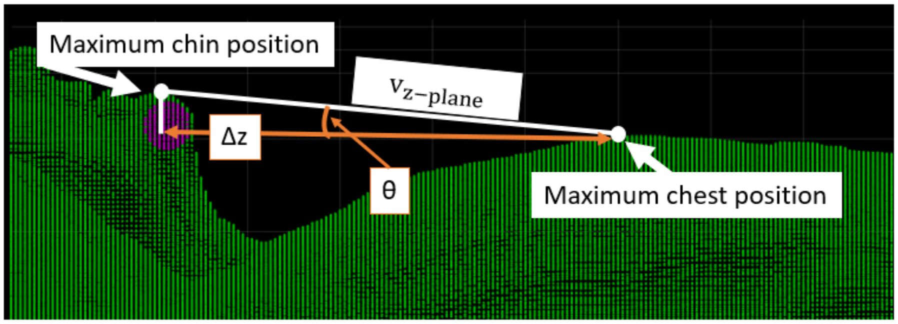

Figure 2.10: A diagram showing an example patient with the maximum chin and chest position, $\Delta z$, $v_{\text{z-plane}}$, and $\Theta$ indicated.

$$T_{xrot} = \begin{bmatrix} 1 & 0 & 0 & 0 \\ 0 & \cos\left(\theta_{CT} - \theta_{SurfaceScan}\right) & \sin\left(\theta_{CT} - \theta_{SurfaceScan}\right) & 0 \\ 0 & -\sin\left(\theta_{CT} - \theta_{SurfaceScan}\right) & \cos\left(\theta_{CT} - \theta_{SurfaceScan}\right) & 0 \\ 0 & 0 & 0 & 1 \end{bmatrix} \tag{2.3}$$

Patient body size and positioning vary, which affects the definition between the patient's chest and chin. Thus the registration algorithm benefits from separately examining the "neck" and "chest" region. First the iterative closest point (ICP) algorithm was applied to the CT "neck" and surface scan "neck" portions. Then the ICP algorithm was applied separately to the CT and surface scan "chest" portions.

The ICP algorithim was developed to efficiently register 3D shapes [78]. One set of points is kept stationary, $\boldsymbol{X} = \{\vec{x_i}\}$, or *fixed*, while the other set of points, the "data" point cloud, is transformed, $\boldsymbol{P} = \{\vec{p_i}\}$, with a combination of translation and rotation. $N_p$ is the number of points in the "data" point cloud. The algorithm seeks to find the local minimum of the mean square objective function, $f(\vec{q})$, (Equation 2.4). For every point in the "data" cloud the closest point in the *fixed* cloud is determined. The value of the mean square objective function is then calculated. An estimate of the translation, $\vec{q_T}$, and rotation matrix, $\vec{q_R}$, is then computed and applied to the "data" point cloud. The closest points are again computed, thereby beginning the cycle again until either a set maximum number of iterations are calculated or until the difference in values between the iterations of transformation matrices has reached a sufficiently small value.

$$f(\vec{q}) = \frac{1}{N_p} \sum_{i=1}^{N_p} ||\vec{x_i} - \boldsymbol{R}(\vec{q_R})\vec{p_i} - \vec{q_T}||^2 \tag{2.4}$$

The ICP algorithm outputs a transformation matrix that was applied to the full surface scan point cloud. Additionally, the root-mean-square error (RMSE) of the Euclidean distance between the aligned point clouds was also output. These results of both the "'chin" and "chest " alignments were then presented to the user and both the resulting match and RMSE values were compared, as seen in examples in Figure 2.11 and 2.12. The most desirable alignment was selected. Desirability was based on both the RMSE value and a visual assessment of the two alignments; this was a subjective choice by the user. In Figure 2.11, the RMSE value was lower for the neck-based alignment, but visually it was clear the chest-based alignment was preferable. In Figure 2.12, the neck-based alignment was deemed superior. The chest alignment resulted in better agreement at level of the patient's chest, but resulted in an angling of the surface scan which tilted the arms in the posterior direction. By selecting the neck-based alignment the arms were placed in a more accurate position and because the CT scan and surface scan were combined the greater height of the CT scan chest was not lost. The CT point cloud and selected registered surface scan were then combined, to create the final patient point cloud. For 6 of the 8 patient scans the chest-based alignment was preferable and this discrepancy highlights the necessity of a human interfacing with the algorithm to make the final decision.

### 2.3.4 Registering Treatment Equipment

Next the treatment equipment was aligned to the patient based off contours exported from the DICOM file. If the patient used a wing board during treatment, then a model acquired by surface scanning the wing board was added to the full-body contour. Because the wing board locks into a fixed position in the SBRT board, the contour of the SBRT board was used to align the wing-board. A wing board model and SBRT board model had been acquired from an in-house CT scan with the wing board locked into the SBRT board. These two components were separately contoured and the wing board contour was augmented using the optical surface scan. After aligning the model of the SBRT board to the SBRT board contour from the patient's CT scan, using the ICP algorithm, the transformation matrix was then applied to the wing board model. This resulted in the wing board being placed in the virtual treatment room such that it was appropriately aligned to the SBRT board.

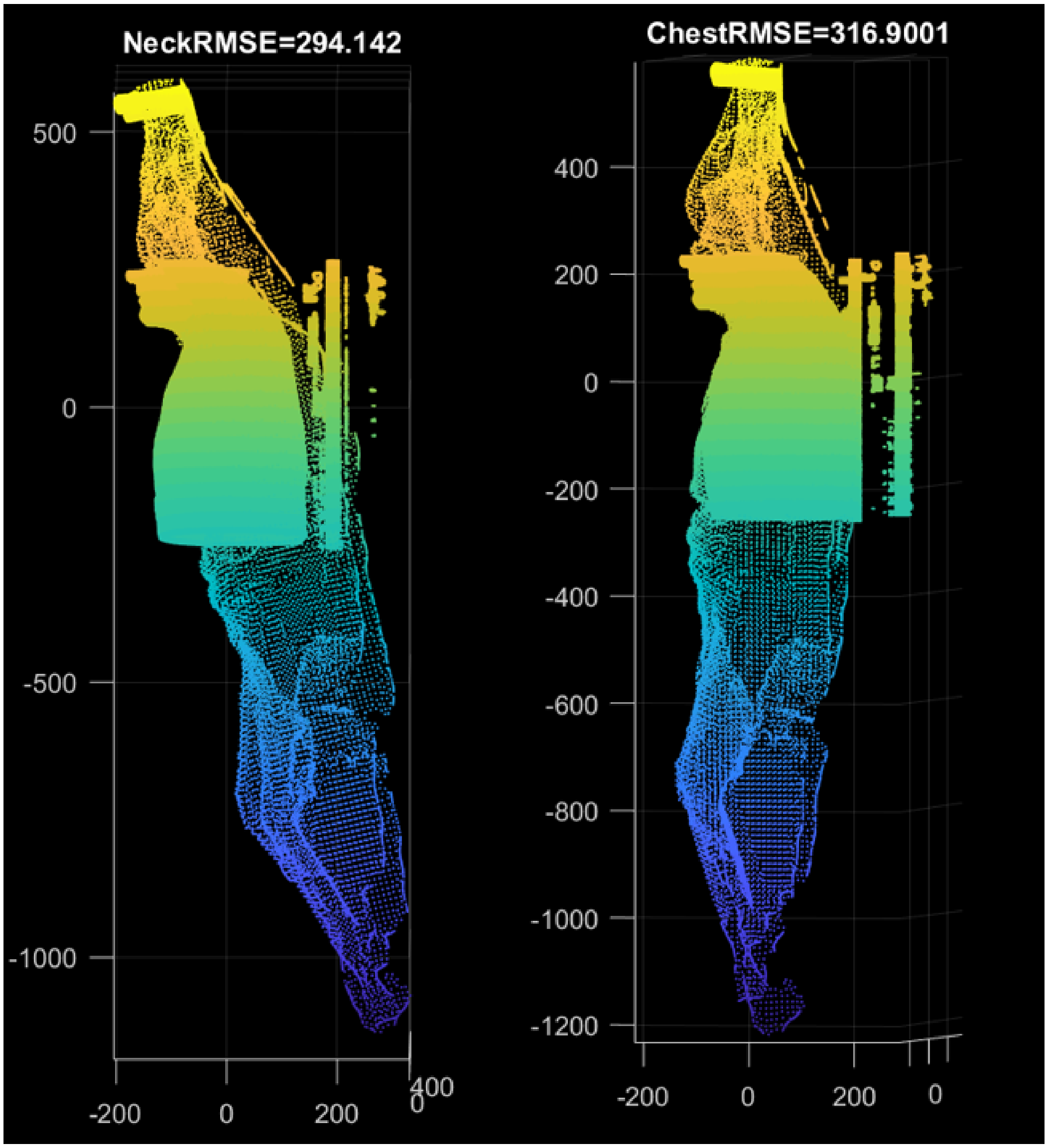

Figure 2.11: An example of the two registered scans which would be presented to the user along with the RMSE values associated with each registration. In this situation, the chest registration (image on the right) was deemed preferable.

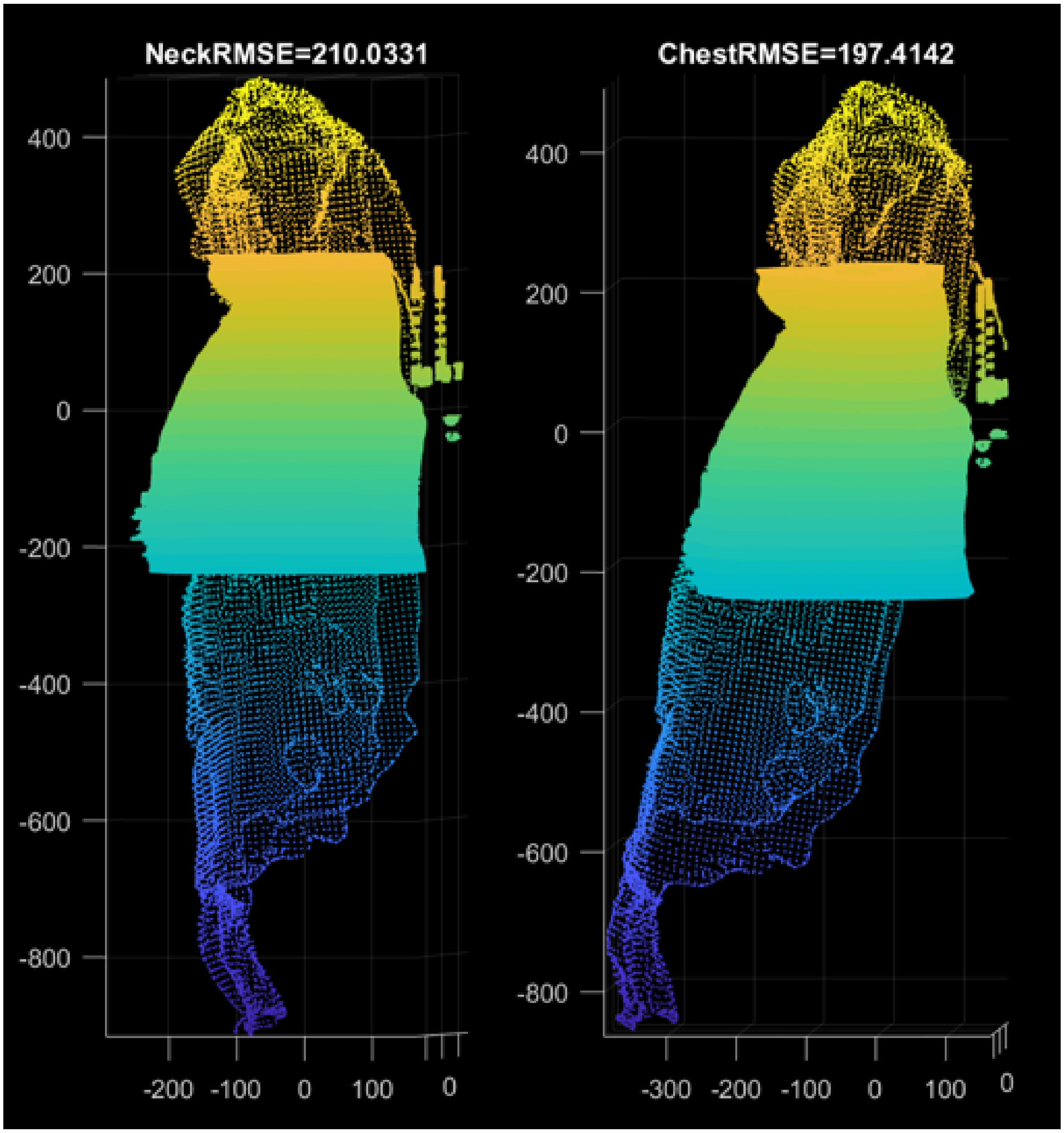

Figure 2.12: An example of the two registered scans which would be presented to the user along with the RMSE values associated with each registration. In this situation, the neck registration (image on the left) was deemed preferable.

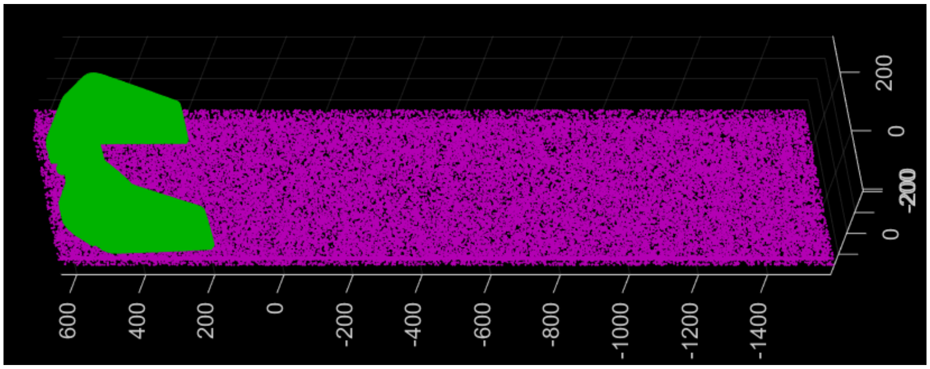

Figure 2.13: The result of aligning the wing board and treatment couch. The couch has been aligned to the couch surface contour from the patient's DICOM file and the superior limit is based the superior limit of the wingboard.

Finally, the couch model was aligned by using the "couch surface" contour that outlines the portion of the treatment couch visible in the CT scan. The model of the treatment couch is an Eclipse contour of the treatment couch repeated until it reached 2 meters in length, which is the length of the actual treatment couch. The ICP algorithm was used to determine the translation matrix which aligned the couch appropriately in the x- and y-dimensions, and the couch was aligned in the z-dimension by matching the end of the couch to the end of the wing board, as shown in Figure 2.13. These final components were then added to the patient point cloud completing the registration process. The patient model now contained the CT scan, the transformed surface scan, the couch, and the wingboard, if applicable.

## 2.4 Collision Detection

### 2.4.1 The Gantry Model

The collision algorithm also utilized the virtual treatment room. A model of a Varian Truebeam Stx LINAC (Varian Medical Systems Inc., Palo Alto, California, United States) [79] gantry head was imported and aligned in the virtual treatment

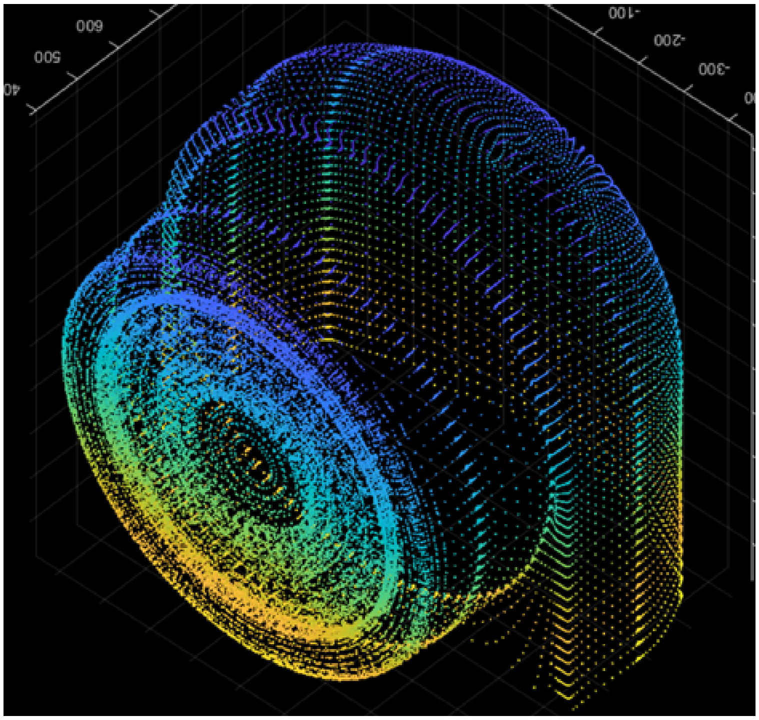

Figure 2.14: An image of the gantry point cloud used in the MATLAB environment that was rotated 360°.

room. To confirm the accuracy of the model's dimensions, the exit window dimensions were measured on both the unit and the model. The difference in dimension was used to scale the gantry head model. Because the LINAC collimator can rotate, the face of the gantry model had been rotated 360° and "smeared" to make it symmetrical and account for every possible treatment position it may adopt (see Figure 2.14). If desired a buffer could be applied, expanding the gantry model outward, to account for error in patient positioning or to provide a safety margin.

### 2.4.2 Bounding Boxes

Collision detection can be computationally expensive if the point clouds are not in some way simplified. There are several simplification methods which trade-off

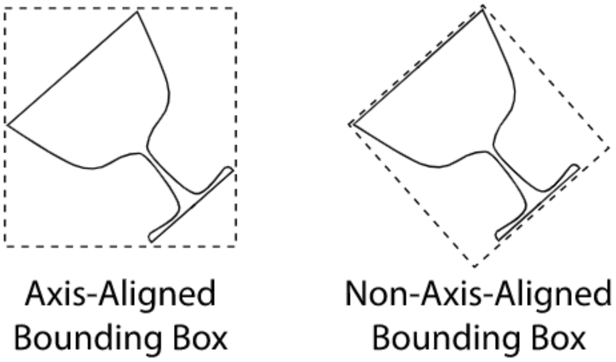

Figure 2.15: A cup encased by an axis aligned bounding box and a non-axis aligned bounding box, or oriented bounding box [80].

accuracy and computational speed. The simplest and quickest method is the use of the axis aligned bounding box (AABB). The point cloud is simplified to a cuboid which encompasses the cloud using its most external points to define the cuboid's boundaries. This cuboid is aligned to the axes which may lead to the cuboid having a much larger volume then the object it contains. This can lead to many false positives. This is especially unhelpful for our application in which we were focused on detecting collision between two objects which were rotated off axis. While slightly more computationally expensive, non-axis aligned or oriented bounding boxes (OBB) allow more accurate collision detection by containing the object within the tightest bounding box possible. OBB are ideal for the modelling of the gantry as the gantry can be modelled as a cuboid. But, approximating the patient geometry as cuboid is insufficient as it would lead to an unacceptable number of false positives. Integrating an OcTree structure (see section 2.4.3) maintained the efficiency of OBB while increasing accuracy.

### 2.4.3 OcTree Structures

OcTree is “a tree data structure in which each internal node has exactly eight children, where a three dimensional space is created by recursively subdividing it into eight octants” [81]. An internal node is a node in a data tree that has at least one child. This structure is applied by initially creating a singular bounding box, the root node, for the entire data structure to be contained; in our application, this was the full body patient point cloud and the immobilization equipment. The root node has eight children, which means the bounding box is subdivided into eight octants. The octants are also OBB, and thus the total volume of the octants may be less than or equal to the volume of the parent OBB. A two dimensional concept of this is illustrated in Figure 2.16. The octants are recursively subdived into further octants until the resulting subdivided octants contains less than or equal to a maximum number of points within the box. While the patient model was transformed into an OcTree, the gantry model was only contained within a single bounding box. Once the contours were simplified, the iterative portion of the algorithm began.

### 2.4.4 Separating Axis Theorem

For each combination of couch and gantry position the following steps, as outlined in Figure 2.17, occurred. First, rotation matrices were applied to the OBBs. The gantry bounding box was rotated to the appropriate position around the z-axis using the transformation matrix shown in Equation 2.5, while the primary patient bounding box was rotated to the appropriate position around the y-axis using the matrix shown in Equation 2.6. The separating axis theorem (SAT) was used to determine whether the OBB overlap.

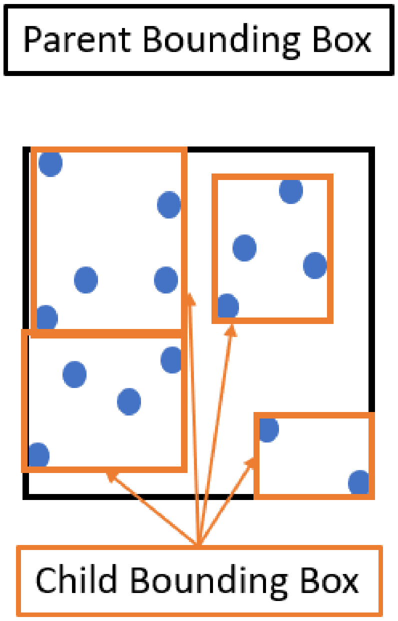

Figure 2.16: An image demonstrating the OcTree structure in two-dimensions. The parent bounding box is the smallest possible volume which can contain the point cloud. The parent box is subdived into quadrants which are then “shrunk” to the smallest volume required to contain the points. Thus, the sum total of the volume of the child boxes may be less than the volume of the parent box.

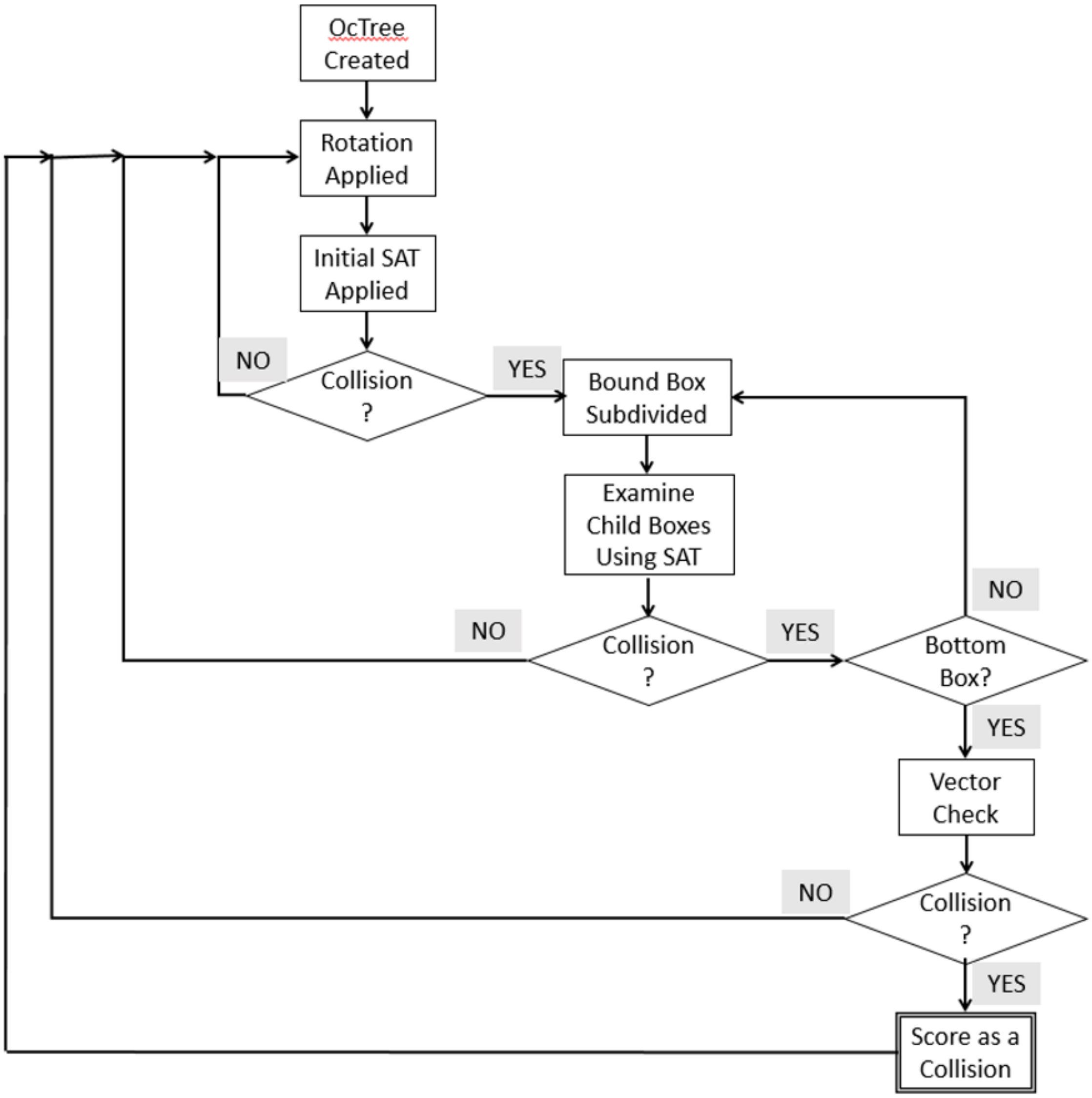

Figure 2.17: Schematic of the collision detection algorithm. This process terminates once all gantry and couch angles are checked for collisions.

$$T_{zrot} = \begin{bmatrix} \cos\theta & \sin\theta & 0 & 0 \\ -\sin\theta & \cos\theta & 0 & 0 \\ 0 & 0 & 1 & 0 \\ 0 & 0 & 0 & 1 \end{bmatrix} \tag{2.5}$$

$$T_{yrot} = \begin{bmatrix} 1 & 0 & 0 & 0 \\ 0 & \cos\theta & \sin\theta & 0 \\ 0 & -\sin\theta & \cos\theta & 0 \\ 0 & 0 & 0 & 1 \end{bmatrix} \tag{2.6}$$

The SAT states that for two cubes in space that if they do not collide there exists a separating plane that is perpendicular to the normal of their surfaces or parallel to the plane spanned by the axes of two cube edges, one edge from each cube [82]. To determine whether this plane exists: a series 16 inequalities are calculated, if one inequality is true, then the dividing plane exists. To calculate the inequalities, the central coordinate, length of the edges, and normal vectors of the cubes' axes were required. The first six inequalities checked to see if a plane parallel to a face of the OBBs divided the OBB. The next ten checked to see if a plane separated the OBB which was spanned by a combination of one axis from each OBB. Because these are simple mathematical operations, determining whether the cubes collide was a rapid process. Thus we could quickly check whether the gantry and initial patient boxes overlap. If they did not, then the next combination of angles was investigated.

If the initial OBB did overlap, then the eight children of the initial patient box were investigated. Each of those child boxes were checked for collision against the gantry OBB using the SAT. If none of the children overlapped, then a new combination of angles was investigated. If one or more child boxes overlapped, then their children were also tested using the SAT. This process repeated until boxes which the SAT determined collided with the LINAC OBB and had no children were found. The final collision check is done on these "bottom" bounding boxes. If a box has no children, it was defined as a "bottom" box. The points within the "bottom" bounding box were extracted and passed to the final collision test, the dot product check. This is to confirm that the collision was not due to a portion of the OBB volumes overlapping while the points contained within the OBBs do not overlap.

### 2.4.5 Dot Product Check

The dot product check is used to determine which side of a plane a point is on. The plane has a unit vector, $\mathbf{\hat{u}} = [\hat{x}, \hat{y}, \hat{z}]$, which originates from a point on the plane $[x_c, y_c, z_c]$. The point is at the coordinates $[x_p, y_p, z_p]$. To complete the check, the vector between the point and the point on the plane, $\vec{\mathbf{v}}$, is calculated (Equation 2.7). Next the dot product of $\mathbf{\hat{u}}$ and $\vec{\mathbf{v}}$ is calculated (Equation 2.8). If the sign of the dot product is positive, then the point is on the same side of the plane which the normal vector points outwards from. A schematic of the vectors is displayed in Figure 2.18.

$$\vec{\mathbf{v}} = \begin{vmatrix} x_c - x_p \\ y_c - y_p \\ z_c - z_p \end{vmatrix} \tag{2.7}$$

$$\mathbf{\hat{u}} \cdot \vec{\mathbf{v}} = \hat{x}(x_c - x_p) + \hat{y}(y_c - y_p) + \hat{z}(z_c - z_p) \tag{2.8}$$

Points contained within the bounding box were tested against the triangles which make up the gantry model. Each triangle had a centre location and normal vector

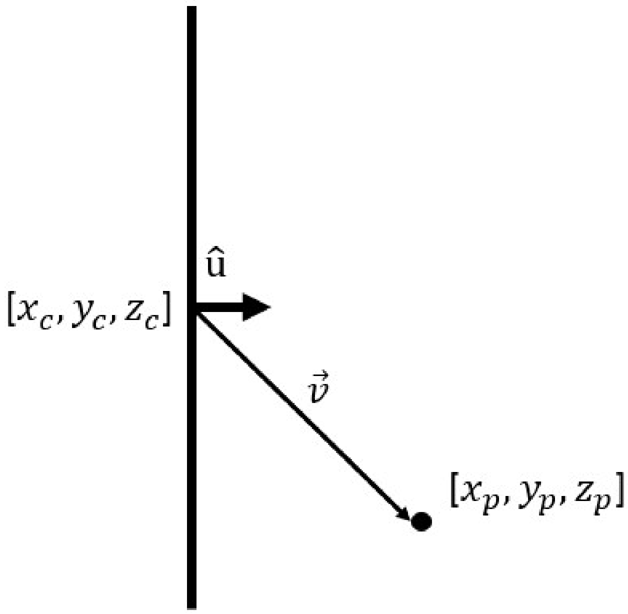

Figure 2.18: A schematic showing an example of the points and vectors used to complete the dot product check. In this example the result of the dot product check would be positive.

originating from the centre. The vectors between each point and a single triangle's centre were calculated. The dot product of each of these vectors with the triangle's normal vector was taken. If the dot product was less then zero then that point was determined to be inside of the gantry and a collision had occurred.

### 2.4.6 Recording a Collision

The collisions were recorded in a 359 x 191 binary array where each element represents one combination of couch and gantry angles. If a collision had occurred, as determined by the dot product being less than one, then the appropriate gantry and couch angle element in the matrix was set to one, else the element was equal to zero. The array is the same size as the overlap maps generated during $4\pi$ calculations. An example of collision zones is shown in Figure 2.19. The coordinate system for couch rotation is illustrated in Figure 2.20 and the coordinate system for gantry rotation is shown in Figure 2.21.

### 2.4.7 Couch-base Collision Zones

Because of the complexity of the motion of the various components which make up the patient support system, the entirety of the couch is not modelled within the virtual treatment room. Thus, it is possible to fail to detect collisions which would occur between the couch base and the gantry. To account for this, these regions of potential collisions were marked as a collision zones. The regions affected can be seen in Figure 2.22. In the cranial collision zone example shown in Figure 2.22, the majority of the space blocked off by the couch base collision zone is less than 30°, which is the minimum arc length allowed within Eclipse, thus the region blocked off was not viable for navigation anyway.

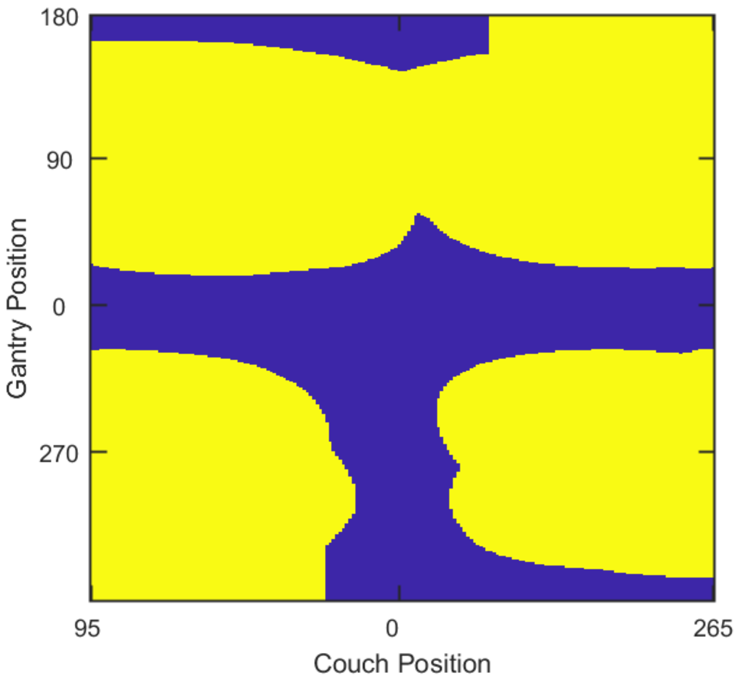

Figure 2.19: An example of SBRT collision zones for a patient with a PTV in the right lung. The yellow regions are the collision zones.

## 2.5 Collision Detection Accuracy

### 2.5.1 Cranial Collision Zones

As part of the testing and development of the collision detection algorithm, a side algorithm which can calculate cranial patient-specific collision zones was developed. This was done by slightly modifying the registration algorithm to align the couch and immobilization components based on the BrainLab (Munich, Germany) infra-red (IR) frame-less array, which is shown in Figure 2.23. Once the couch and immobilization equipment were aligned, the patient contour was extended by repeating the most inferior transverse slice of the CT until the end of the couch. This was done to account for the patient's chest and arms not captured within the CT scan. The goal of this was to determine the accuracy of the collision detection

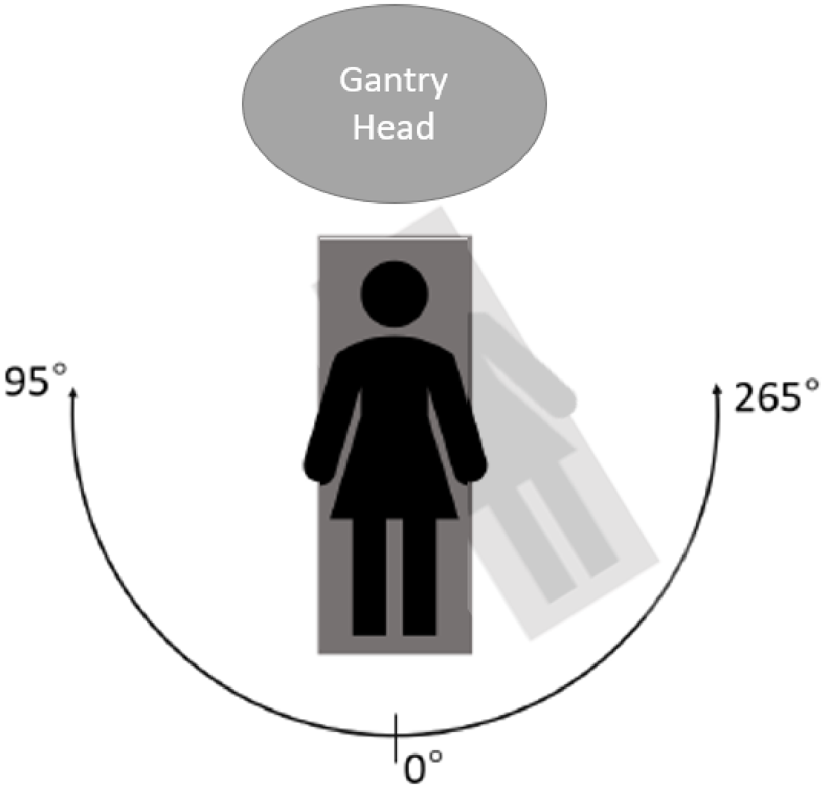

Figure 2.20: An illustration of the couch rotation coordinate system.

algorithm. While a difference exists between the cranial and extra-cranial methods, the collision detection methodology is the same, thus the applicability of the accuracy measurement.

### 2.5.2 Effect of Patient-Specific Collision Zones

For eight cranial test patients, collision zones and overlap maps were calculated. Then for each patient their $4\pi$ trajectories were calculated twice, once with their specific collision zones and once with the collision zones manually measured for MacDonald *et al.*'s work [41]. Both sets of collision zones were determined with a buffer of 3 cm applied. The arc trajectories were imported into the Eclipse treatment planning system (v13.6) and inverse optimized with VMAT (PRO v11.1

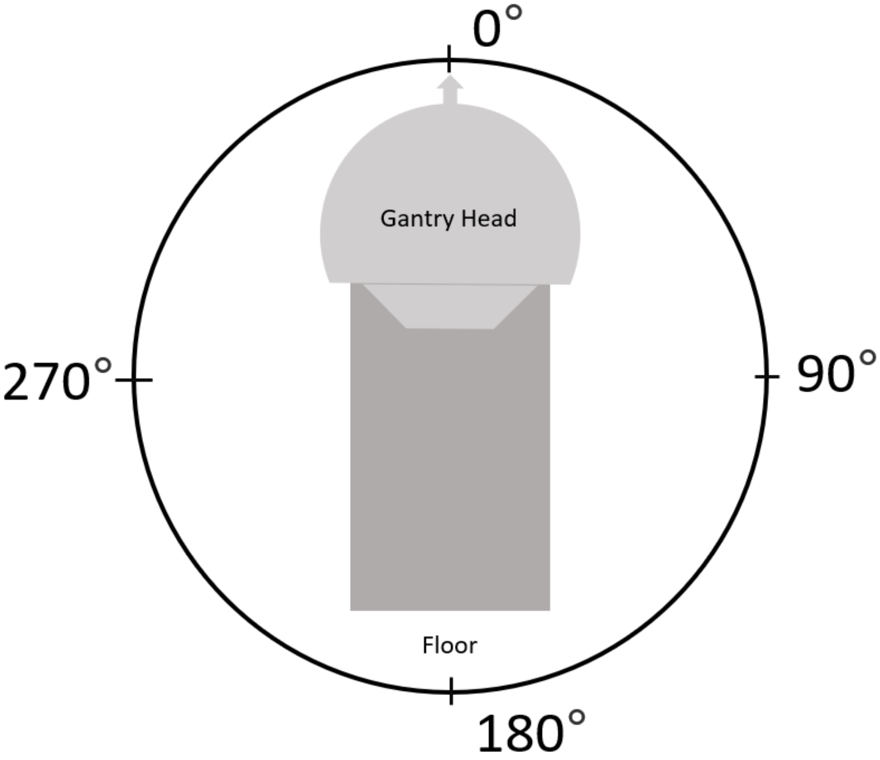

Figure 2.21: An illustration of the gantry rotation coordinate system.

or PRO v13.6) to clinical standards. Final dose was calculated with AAA (v11.1 or v13.6) and a dose calculation grid size of 1.5 mm. The mean and maximum dose to several OARs, the conformity index of the PTVs, the overlap scores, and trajectories were compared between the two plans. The OARs examined were: the brainstem, chiasm, eyes, lens, and the optic nerves (without any margins). The conformity index refers to the volume contained by a reference isodose line divided by the total PTV volume [84]. The reference isodose line was 90% of the prescribed dose and the same between the patient's two treatment plans. Overlap score is the sum of the overlap values from the overlap map that the treatment arcs pass through, and this is the value the $4\pi$ algorithm seeks to minimize [41]. Additionally, the efficacy of using a singular collision zone for all patients was tested, by overlaying the trajectories generated with general collision zones onto the patient-specific maps. This informed if collisions would have occurred if a general

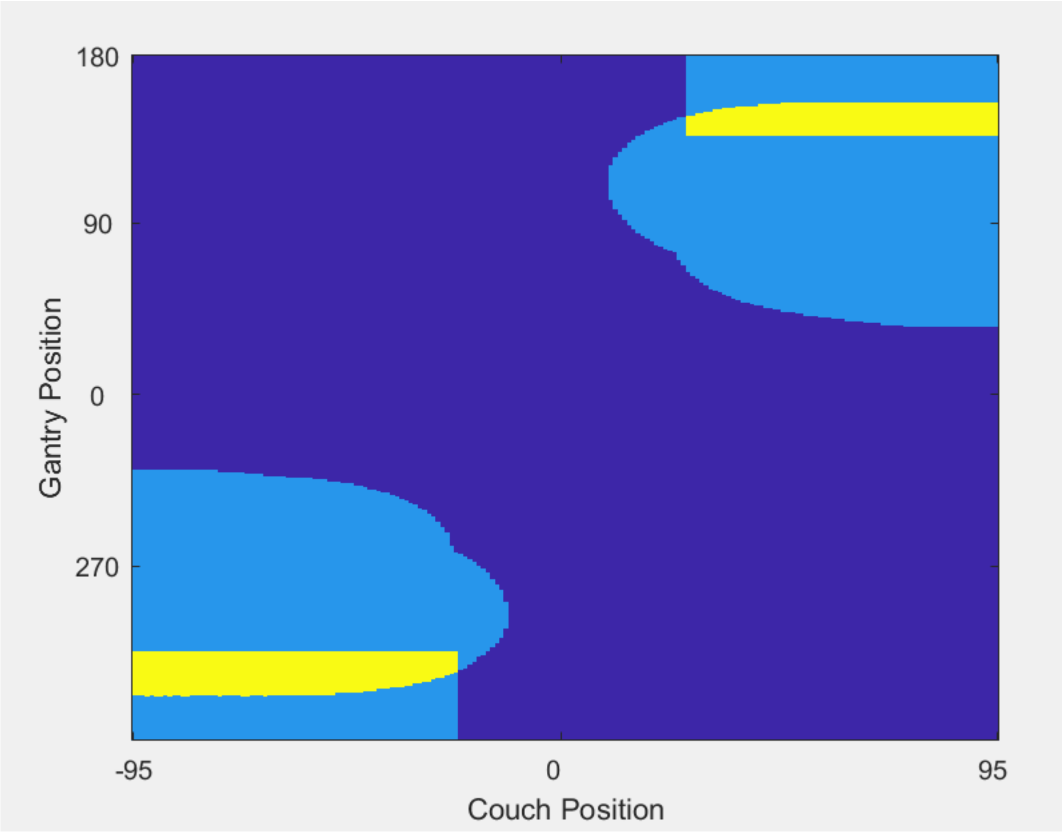

Figure 2.22: An overlap map with a cranial collision zones and the couch base collision zones overlaid. The yellow region indicates the overlap between the two sets of collision zones. The region covered by the rectangular couch base collision zones which was not previously covered by the cranial collision zones was primarily less than 30° thus could not be navigated by the $4\pi$ algorithm.

collision zone map was used for delivery.

### 2.5.3 End-to-End Testing

To assess the accuracy of the collision detection portion of the algorithm, an end-to-end test was preformed using a MAX-HD™SRS phantom (Integrated Medical Technologies, inc. Troy, New York, USA) that was placed at the neck of a RANDO phantom (Radiology Support Devices Inc., East Dominguez Street Long Beach, California, USA). A thermoplastic mask was crafted for the MAX-HD™phantom

Figure 2.23: An image of the BrainLab IR frame-less array [83].

and the combined phantoms were CT scanned and contoured as if they were a SRS patient (see Figure 2.24).

The collision detection algorithm was used to generate cranial collision zones with a 3 cm buffer. Using the PTV contour, image guided alignment based on a cone-beam CT ensured the proper alignment of the phantom set-up on the treatment couch for manual collision zone measurement. The collision zones were then measured with a 3 cm buffer. The measured and calculated collision zones were overlaid to determine the accuracy, sensitivity, and negative predictive value (NPV) of the collision detection algorithm. A confusion matrix, seen in Table 2.1, defines the values extracted from the maps: the true positive (TP), false positive (FP), true negative (TN), and false negative (FN) values. The equations for accuracy, sensitivity, and NPV are shown in Equation 2.9, 2.10, and 2.11 respectively. The reason we consider NPV is that it goes to unity when there are no false negatives, and false negatives will result in a collision as the algorithm has failed to calculate a real collision that would have occurred on the treatment unit. Accuracy indicates how well the calculated collision zones match the collision zones. Higher accuracy means $4\pi$ algorithm has the most accurate map through which to navigate. Sensitivity is examined as it goes to unity when we have captured every possible collision during the collision zone calculation.

| | | Measured Collision Zone | |
|---|---|---|---|
| | | Collision Occurred | Collision Didn't Occur |
| Calculated Collision Zone | Collision Occurred | TP | FP |
| | Collision Didn't Occur | FN | TN |

Table 2.1: Confusion matrix used to calculate the collision detection accuracy values.

$$\text{accuracy} = \frac{\text{TP} + \text{TN}}{\text{TP} + \text{TN} + \text{FP} + \text{FN}} \tag{2.9}$$

Figure 2.24: Image of the phantom set-up which used for the end-to-end test for collision detection accuracy.

$$\text{sensitivity} = \frac{\text{TP}}{\text{TP} + \text{FN}} \tag{2.10}$$

$$\text{NPV} = \frac{\text{TN}}{\text{TN} + \text{FN}} \tag{2.11}$$

## 2.6 Registration Accuracy

To determine the accuracy of the registration algorithm required the creation of “true” collision zones for eight test patients. These eight patients were from the cohort which was surface scanned (N=11). Three patients were eliminated for the following reason: one was the only patient scanned with their arms by their side and thus had no potential match in the library, one was a liver SBRT patient, and the final one did not end-up receiving lung SBRT treatment. The “true” collision zone was calculated with the patient’s own surface scan being registered to the patient’s own CT to create the full body contour with a zero cm buffer applied. By not applying a buffer to the “true” collision zone it became possible to determine which buffer size needs to applied to the ”clinical” collision zone to assure safe treatment delivery. A “clinical” collision zone is the registration collision zone, which was calculated with the patient’s own surface scan excluded from the library to simulate clinical application. These collision zones were calculated with 0, 3, and 6 cm buffers applied. Next, the “true” and “clinical” collision zones were overlaid to test the accuracy of the registration algorithm. The confusion matrix, seen in Table 2.2, defines the values extracted from that graph. For each patient, the sensitivity, or true positive rate (TPR), and false positive rate (FPR) were calculated using Equations 2.10 and 2.12. These values were then plotted in receiver operating characteristic (ROC) space.

| | | “True” Collision Zone | |
|---|---|---|---|
| | | Collision Occurred | Collision Didn’t Occur |
| Clinical Collision Zone | Collision Occurred | TP | FP |
| | Collision Didn’t Occur | FN | TN |

Table 2.2: Confusion matrix used to calculate the registration accuracy values.

$$\mathrm{FPR} = \frac{\mathrm{FP}}{\mathrm{FP} + \mathrm{TN}} \tag{2.12}$$

## 2.7 Comparison of Conventional and Optimized Trajectories for SBRT

The final test was comparing whether the trajectories generated using the $4\pi$ methodology with patient-specific collision zones produced improved dosimeteric outcomes when compared to the current clinical standard of SBRT. The same patients used for the registration accuracy test (N=8) were used for this testing. After the patient-specific collision zones were calculated, the overlap maps were calculated by a simplified version of the methodology employed by MacDonald and Thomas [41] (without OAR weighting or foreground/background weighting factors). By integrating the collision zones into the overlap map, it was prepared for the trajectory generation algorithm. The regions of the collision zone were set to infinite overlap in order to force the trajectory algorithm to avoid these regions.

The arcs were generated using a modified Bellman-Ford algorithm which computes the shortest path through a graph; the length between the vertices of the graph are the overlap scores [85]. The algorithm seeks to minimize the sum overlap value incurred by navigating the overlap map while maintaining deliverability. Eclipse treatment planning system necessitates the following limitations: the maximum number of sub arcs is 10, and the minimum sub arc length was 30° of gantry span. The arc trajectories were imported into the Eclipse treatment planning system (v13.6) and inverse optimized with VMAT (PRO v11.1 or v13.6) according to clinical standards by a co-author, a medical physicist with six years of experience in SBRT treatment planning. The clinical treatment plans had been generated by an equally experienced medical physics team member. Both plans were planned to be delivered on a Varian TrueBeam STx LINAC with 6MV flattening filter free photon beam. The prescribed dose, either 24 or 36 Gy, and reference isodose, 90% of the prescribed dose, were maintained between the two plans. Both plans were optimized with the same objectives and either the AAA v11.1 or AAA v13.6 dose calculation algorithm was used with a dose calculation grid size of 1.5 mm. The mean and maximum dose to several OARs, the conformity index of the PTVs, and the overlap scores were compared between the clinical and $4\pi$ optimized plans. The OARs relevant to lung SBRT treatments are: the right and left lungs, the trachea PRV, the esophagus PRV, the large bronchus, the aorta, the heart/pericardium, and the spinal cord PRV.

# Chapter 3

# Results

## 3.1 Effects of patient-specific Collision Zones on $4\pi$ SRS

### 3.1.1 Dosimeteric Consequences of patient-specific Collision Zones

The maximum and mean dose to the cranial patient's OARs were extracted from Eclipse. A Wilcoxon signed-rank test was used to assess whether a statistically significant change to the dose occurred when the patient-specific collision zones were applied. This statistic test was used as the data could not be assumed to have a normal distribution, but the data was paired and came from the same population. The resulting p-values are displayed in Table 3.1.1. Outside of the maximum dose to the right eye and the mean dose to the chiasm, the change in mean and maximum dose to the OARs was statistically insignificant ($p > 0.05$). Additionally, the overlap scores from the two sets $4\pi$ maps and the PTV conformity index were compared. There was found to be statistically significant difference in the overlap scores ($p=0.017$) but not for the PTV conformity index ($p=0.207$). One patient's general and specific collision $4\pi$ maps are displayed in Figure 3.1.

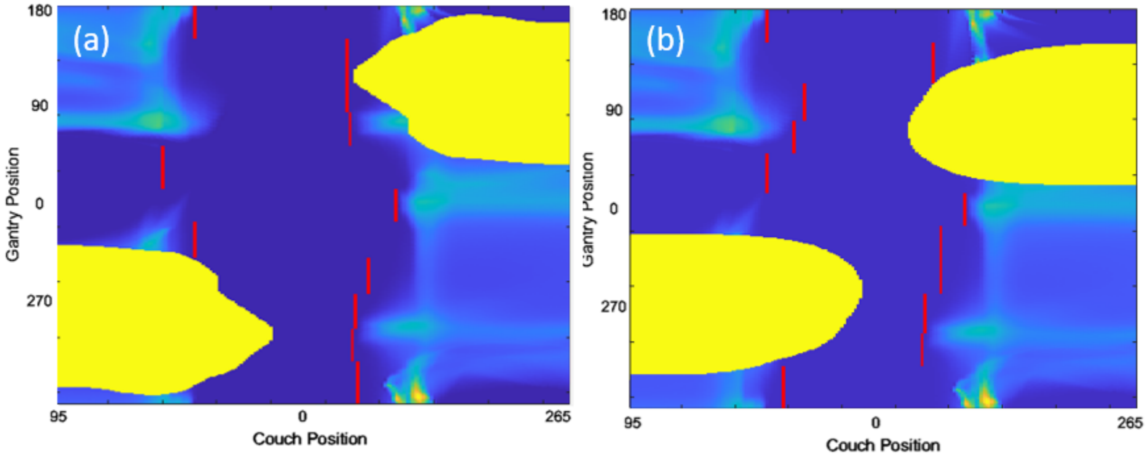

Figure 3.1: $4\pi$ overlaps maps demonstrating: (a) general collision zone with generated treatment trajectories and (b) patient-specific collision zone with generated treatment trajectories for an example patient.

| OAR | Maximum dose p-value | Mean dose p-value |
|---|---|---|
| Brainstem | 0.58 | 0.40 |
| Chiasm | 0.21 | 0.034 * |
| Right Eye | 0.02 * | 0.13 |
| Left Eye | 0.48 | 0.34 |
| Right Lens | 0.33 | 0.47 |
| Left Lens | 0.58 | 0.31 |
| Right Optics Nerve | 0.40 | 0.16 |
| Left Optics Nerve | 0.32 | 0.44 |

* Statistically significant at $p < 0.05$.

Table 3.1: p-values for the change in the maximum and mean percentage doses to cranial OARs as calculated by the Wilcoxon signed-rank test (N = 8).

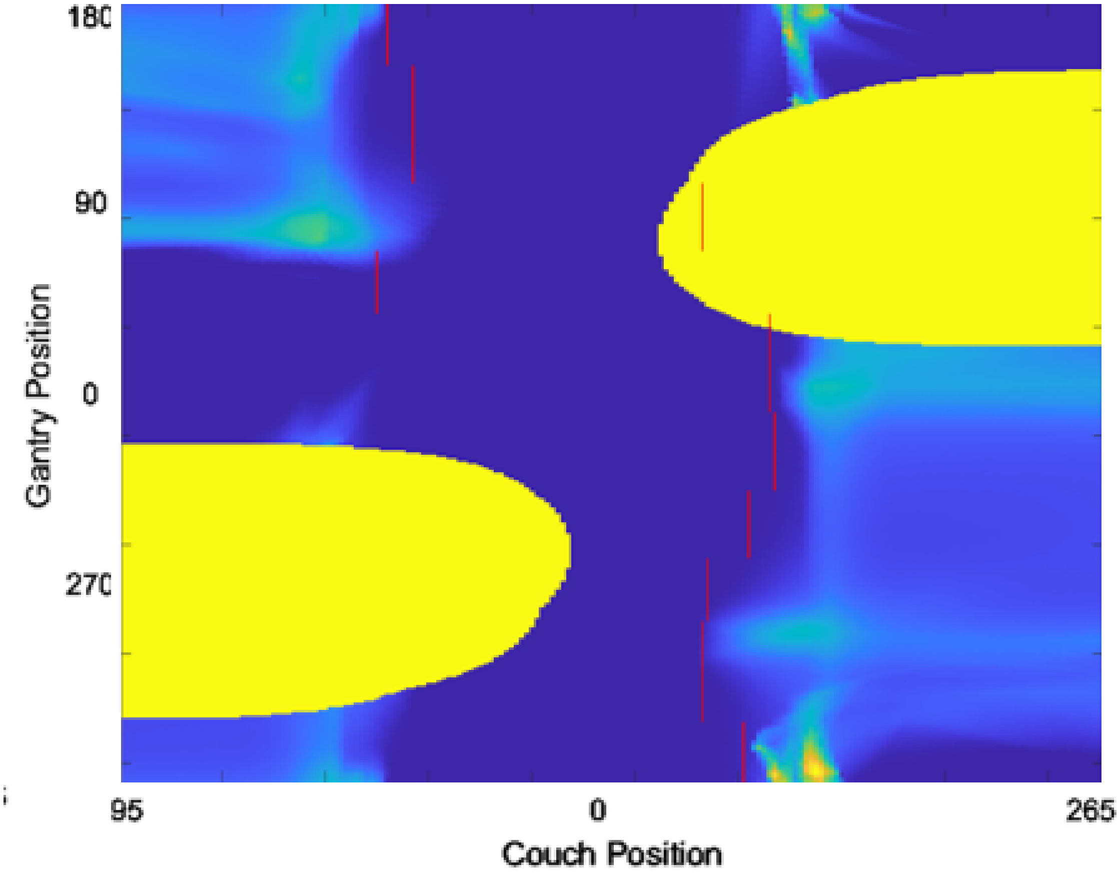

Figure 3.2: An example of one patient's trajectories generated using the general collision zones overlaying their patient-specific collision zones for an example patient. Note that the treatment arcs intersect with the collision zones.

### 3.1.2 Consequences of using General Collision Zones

At least one possible collision was identified for seven out of the eight patients if the general arc trajectories were delivered. Figure 3.2 shows treatment arcs generated using a general collision zone overlaid onto the patient-specific overlap map for an example patient. These treatment arcs overlap with the patient-specific collision zone and thus would lead to collisions.

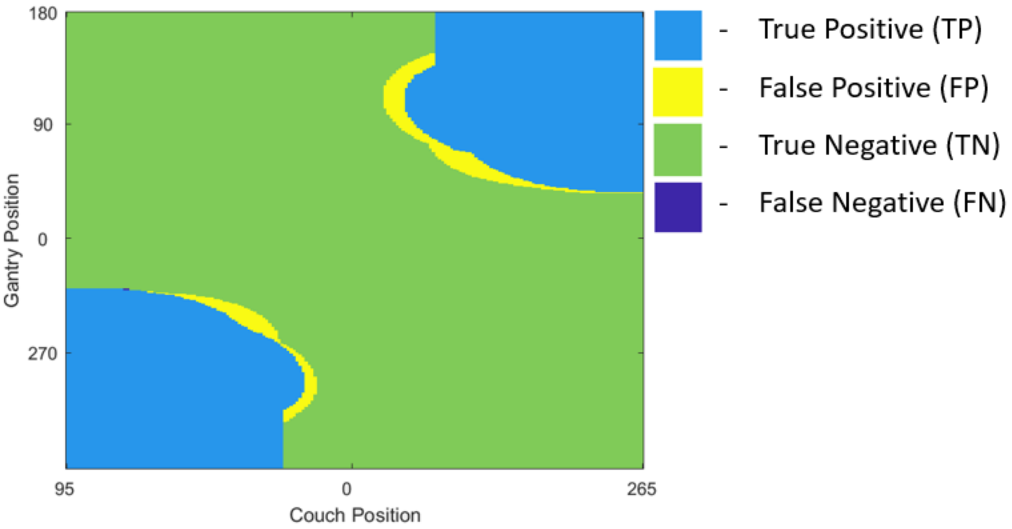

Figure 3.3: Manually measured and calculated cranial end-to-end collision zones overlaid. The collision zones were measured and calculated with a 3 cm buffer.

## 3.2 Collision Detection Accuracy

The results of the end-to-end testing are displayed in Figure 3.3. A 3 cm buffer resulted in a 99.99% sensitivity and 99.99% NPV. The accuracy was calculated to be 97.8%. Every combination of couch and gantry angle was tested. This is important to note when comparing the results to Mann *et al.*'s results in which they also used a 3 cm buffer, in which only 13 couch angles were tested ranging from 90 to 270° with 15° intervals for five different PTV locations [71]. Both sets of results are outlined in Table 3.2.

## 3.3 Registration Accuracy

The results of comparing the “true” collision zones, registering the matching patient surface scan to the patient’s CT scan, to the clinical collision zones, selecting a surface scan as though the patient had not been surfaced scanned, are

| | TP\|TN\|FP\|FN | Accuracy (%) | Sensitivity (%) | NPV (%) |
|---|---|---|---|---|
| Our End-to-End Test | 18995\|48281\|1482\|2 | 97.8 | 99.99 | 99.99 |
| PTV 1* | 62\|697\|12\|0 | 98.4 | 100 | 100 |
| PTV 2* | 11\|629\|19\|0 | 97.1 | 100 | 100 |
| PTV 3* | 11\|638\|32\|0 | 95.3 | 100 | 100 |
| PTV 4* | 11\|629\|21\|0 | 96.8 | 100 | 100 |
| PTV 5* | 11\|643\|40\|0 | 94.2 | 100 | 100 |

* Results from Mann *et al.*'s paper [71].

Table 3.2: Receiver operating characteristic results for the end-to-end cranial collision testing as well as the results from Mann *et al.*'s work [71]. For both Mann *et al.*'s work and ours the collision zones were calculated and measured with a 3 cm buffer. Accuracy is given by the sum of true positive (TP) and true negative (TN) results divided by the total for all results. Sensitivity, or the true positive ratio (TPR) = TP/(TP+FN) and the negative predictive value (NPV) = TN/(TN + FN) achieves unity for no false negative (FN) results.

displayed in Table 3.3. Additionally, the results are displayed in Figure 3.4 in ROC space. Increasing the buffer size resulted in an increase in sensitivity and NPV values for all patients. The increased NPV meant there were fewer false negatives, but this corresponded to decreased accuracy for each patient. The average accuracy decreased from 91.63 ± 1.94% to 86.29 ± 2.38% between the 3 cm and 6 cm buffer size. The average NPV increased from 97.09 ± 2.38% to 98.74 ± 1.55% between the same buffer sizes. Additionally, the sensitivity values increased from 98.20 ± 1.44% to 99.34 ± 00.82%.

### 3.4 Comparison of Conventional and Optimized Trajectories for SBRT

The maximum and mean dose to each OAR for both conventional and optimized SBRT trajectories are shown in Figures 3.5 and 3.6. These are results from a single patient who demonstrated the best-case result for change in dose to OARs. Figure 3.7 and 3.8 show the percentage dose change to the OARs achieved by optimizing the treatment trajectories, averaged over all patients (N=8). The change in dose is

| Patient | Buffer Size | | | | | | | | |
|---|---|---|---|---|---|---|---|---|---|
| | 0 cm Buffer | | | 3 cm Buffer | | | 6 cm Buffer | | |
| | Accuracy (%) | Sensitivity (%) | NPV (%) | Accuracy (%) | Sensitivity (%) | NPV (%) | Accuracy (%) | Sensitivity (%) | NPV (%) |
| Patient 1 | 95.51 | 94.62 | 92.32 | 93.28 | 97.93 | 96.53 | 89.16 | 99.80 | 99.59 |
| Patient 2 | 93.52 | 97.51 | 96.22 | 91.33 | 98.90 | 98.14 | 82.89 | 99.87 | 99.70 |
| Patient 3 | 90.41 | 94.00 | 90.41 | 87.34 | 96.37 | 93.12 | 83.57 | 98.45 | 96.35 |
| Patient 4 | 93.81 | 94.43 | 92.78 | 91.34 | 96.63 | 95.08 | 88.28 | 98.22 | 97.02 |
| Patient 5 | 96.14 | 95.49 | 94.34 | 93.03 | 96.87 | 95.61 | 88.64 | 98.40 | 97.37 |
| Patient 6 | 95.31 | 97.78 | 96.86 | 91.27 | 99.55 | 99.24 | 86.07 | 99.97 | 99.94 |
| Patient 7 | 97.26 | 97.61 | 96.53 | 92.17 | 99.69 | 99.44 | 84.74 | 100 | 100 |
| Patient 8 | 96.67 | 96.87 | 95.88 | 93.24 | 99.70 | 99.54 | 86.96 | 100 | 100 |
| **Average** | **94.83** | **96.04** | **94.42** | **91.63** | **98.20** | **97.09** | **86.29** | **99.34** | **98.74** |

Table 3.3: Receiver operating characteristic results for the registration algorithm accuracy comparisons, the accuracy values decrease while the sensitivity and the negative predictive values (NPV) increase as the buffer size increased. Accuracy is given by the sum of true positive (TP) and true negative (TN) results divided by the total for all results. Sensitivity, or the true positive ratio (TPR) = TP/(TP+FN) and the negative predictive value (NPV) = TN/(TN + FN) achieves unity for no false negative (FN) results.

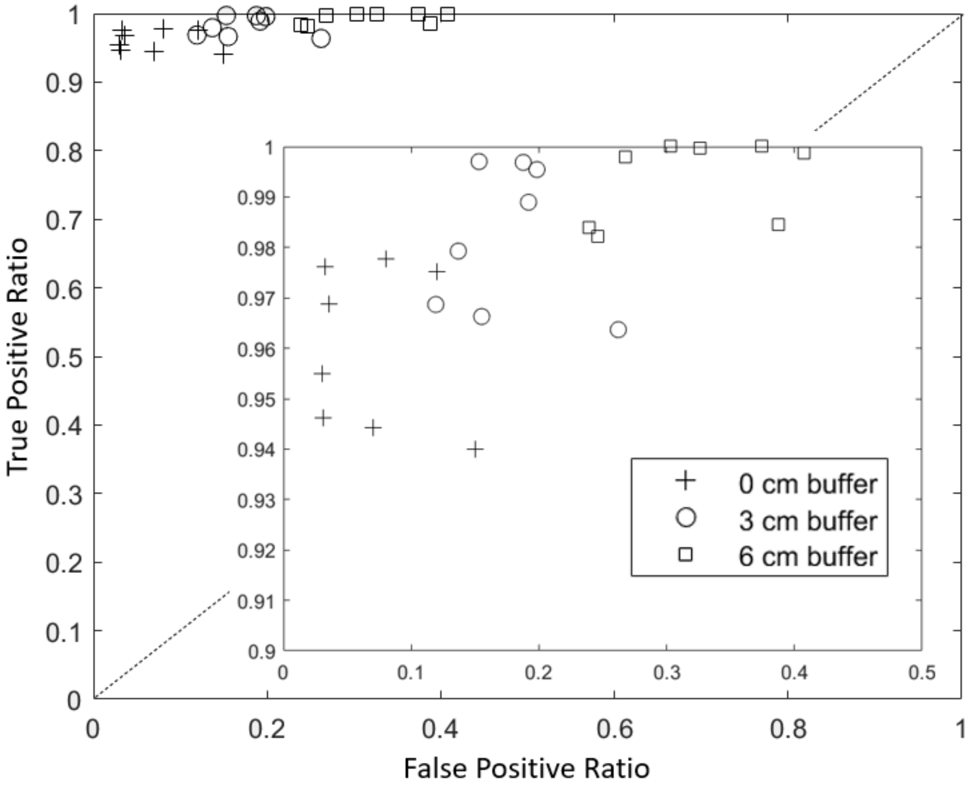

Figure 3.4: Receiver operating characteristic plot for the 0, 3, and 6 cm buffer results for the eight test patients.

represented in percentage dose because the patient's prescribed dose varied, thus using absolute dose would not have accurately reflected the results. The change in percentage dose is calculated by extracting the relative dose values for each OAR from Eclipse for both the clinical and $4\pi$ SBRT plans, and then subtracting the $4\pi$ plan relative dose from the clinical SBRT relative dose. Although there are very large error bars, for the majority of organs a decrease was seen in the mean and maximum percentage dose. The average dose values for each OAR, as well as the normalized improvement, is presented in Table 3.4. Normalized improvement is calculated by dividing the difference between the values by the initial values, thus better representing the actual improvement achieved.

To determine if a statistically significant change to dose was achieved, a Wilcoxon rank-sum test was performed, and the p-values are displayed in Table 3.5. No statistically significant ($p < 0.05$) change to the maximum dose to any organ was found. When examining the change in mean dose to OARs, the only statistically significant change was in the dose to the ipsilateral lung ($p=0.04$) and the contralateral lung ($p=0.04$). The ipsilateral lung saw a 0.7 % increase in dose while the contralateral lung saw a 0.55 % decrease. The mean PTV conformity index was $1.08 \pm 0.02$ for conventional trajectory plans and $1.09 \pm 0.03$ for the optimized trajectory plans, and no statistically significant difference was found between them ($p=0.13$).

When the patient's clinical treatment arcs were placed on the patient's overlap map and compared to the patient-specific treatment arcs, the clinical arc passed directly through regions with high overlap scores, as can be seen in Figure 3.9 for an example case. This is reflected in the overlap score comparison where a statistically significant decrease in overlap score was found ($p=0.012$). In fact, every patient saw a decrease in overlap score when the patient-specific arcs were used. The

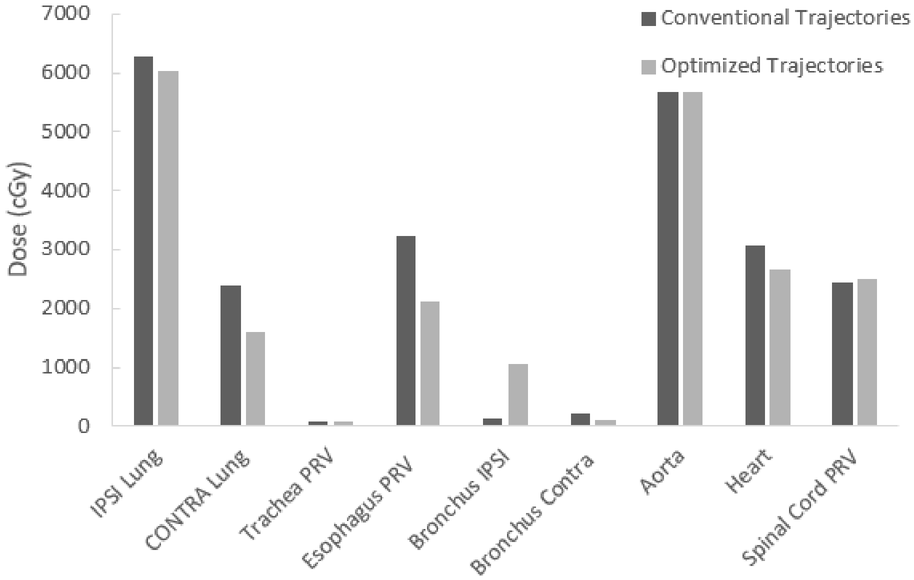

Figure 3.5: Maximum dose to OARs for an example lung test-patient shown for both conventional and $4\pi$ optimized trajectories. The majority of the OARs do see a decrease in maximum dose, aside from the ipsilateral bronchus.

normalized mean percentage decrease was $51.82 \pm 24.48\%$.

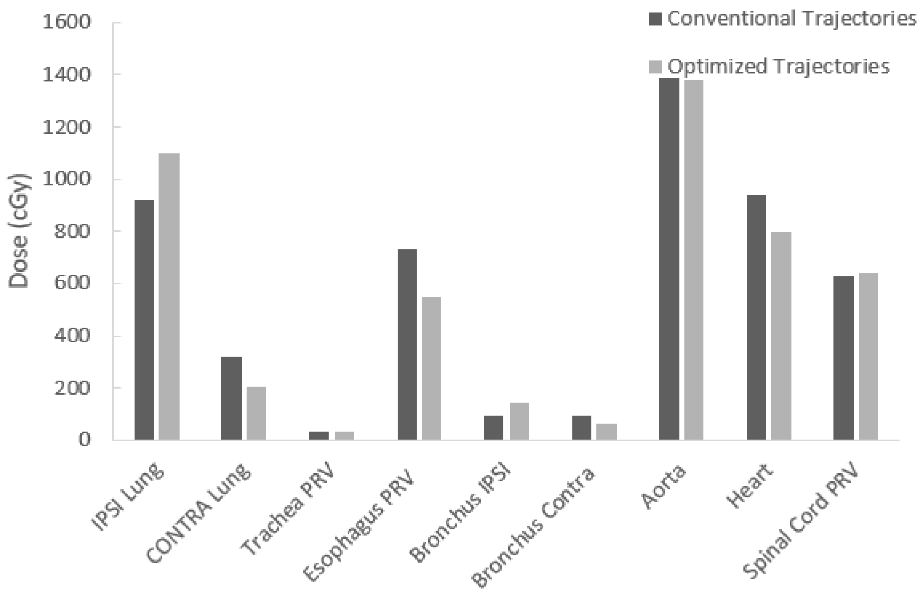

Figure 3.6: Mean dose to OARs for an example lung test-patient shown for both conventional and $4\pi$ optimized trajectories. Aside from the ipsilateral bronchus and the ipsilateral lung, a decrease in the mean dose is seen.

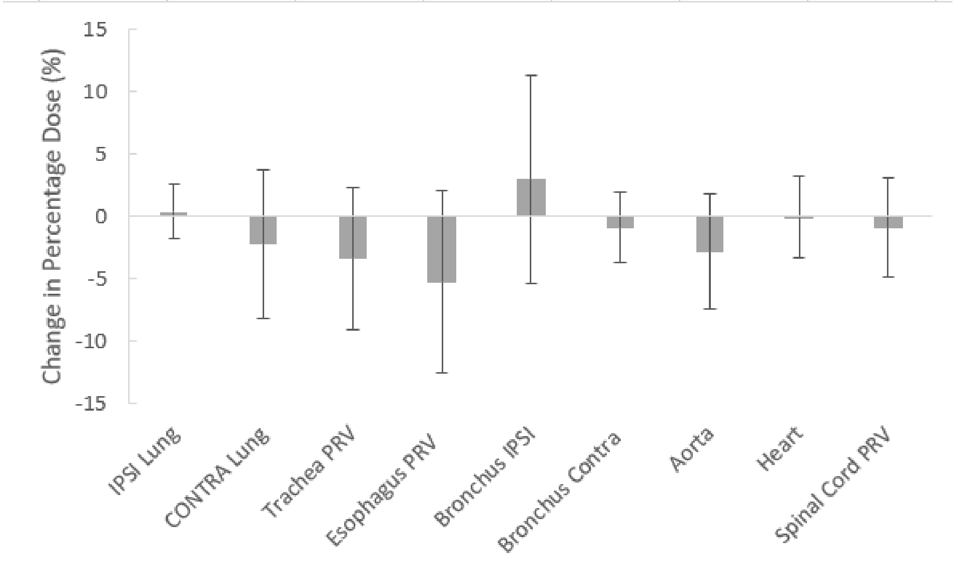

Figure 3.7: Mean change in percentage maximum dose for entire patient population (N = 8), with error bars representing the standard deviation. The change in percentage dose is the $4\pi$ optimized treatment plan OARs' relative dose minus the clinical treatment plan OARs' relative dose. Thus a negative value indicates an improvement achieved using the $4\pi$ methodology.

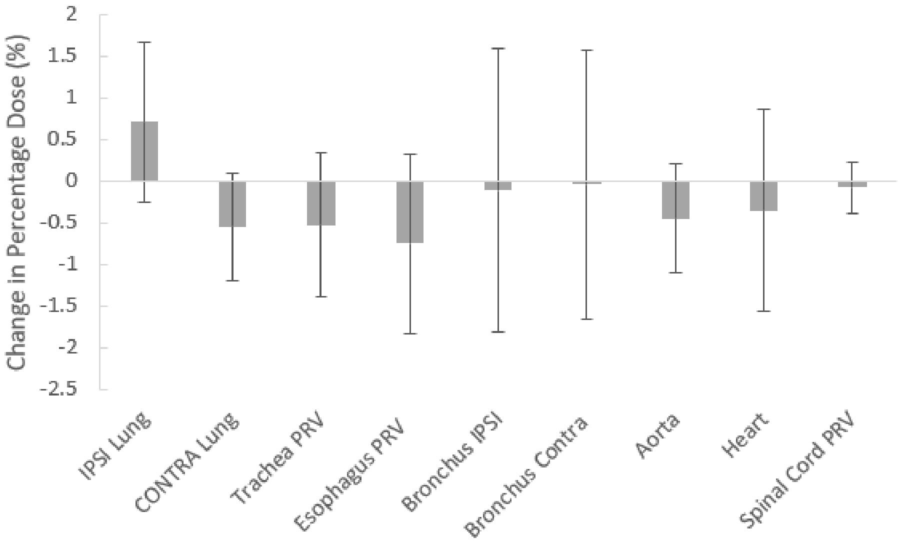

Figure 3.8: Mean change in percentage mean dose for entire patient population (N = 8), with error bars representing the standard deviation. The change in percentage dose is the $4\pi$ optimized treatment plan OARs' relative dose minus the clinical treatment plan OARs' relative dose. Thus a negative value indicates an improvement achieved using the $4\pi$ methodology.

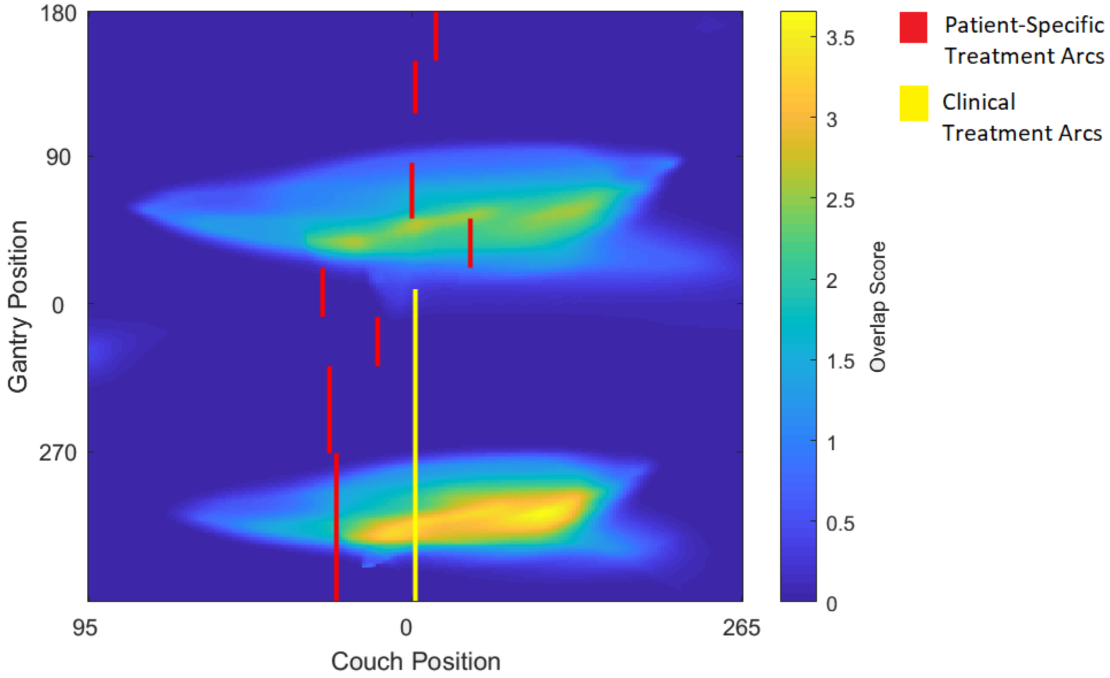

Figure 3.9: An example of a patient's clinical and $4\pi$ patient-specific treatment arcs overlaid on the patient's overlap map. The patient-specific arcs are informed by collision zones which have not been included in this image.

| | Conventional Trajectories (%) | Optimized Trajectories (%) | Improvement (%) | Normalized Improvement (%) | Normalized Improvement [Langhan *et al.* data ] (%) | Normalized Improvement [Dong *et al.* data ] (%) |
|---|---|---|---|---|---|---|
| Ipsilateral Lung $D_{max}$ | $100.59 \pm 1.91$ | $101.00 \pm 1.49$ | -0.41 | -0.41 | | |
| Ipsilateral Lung $D_{mean}$ | $8.80 \pm 3.95$ | $9.51 \pm 4.46$ | -0.71 | -8.10 | 18.85 | |
| Contralateral Lung $D_{max}$ | $18.98 \pm 10.23$ | $16.79 \pm 9.03$ | 2.19 | 11.53 | | |
| Contralateral Lung $D_{mean}$ | $2.00 \pm 1.45$ | $1.45 \pm 1.21$ | 0.55 | 27.50 | 42.86 | |
| Ipsilateral Bronchus $D_{max}$ | $9.23 \pm 17.30$ | $12.23 \pm 23.67$ | -3.00 | -32.52 | | 44 |
| Ipsilateral Bronchus $D_{mean}$ | $2.19 \pm 2.52$ | $2.08 \pm 3.21$ | 0.11 | 5.14 | | |
| Contralateral Bronchus $D_{max}$ | $3.53 \pm 3.28$ | $2.61 \pm 4.64$ | 0.91 | 25.89 | | 44 |
| Contralateral Bronchus $D_{mean}$ | $1.43 \pm 1.24$ | $1.39 \pm 2.41$ | 0.04 | 2.63 | | |
| Trachea $D_{max}$ | $15.93 \pm 16.68$ | $12.58 \pm 12.88$ | 3.35 | 21.04 | | 37 |
| Trachea $D_{mean}$ | $3.56 \pm 4.95$ | $3.04 \pm 4.17$ | 0.53 | 14.74 | | |
| Esophagus $D_{max}$ | $24.06 \pm 15.$ | $18.83 \pm 12.85$ | 5.24 | 21.77 | 5.26 | 72 |
| Esophagus $D_{mean}$ | $3.83 \pm 3.47$ | $3.08 \pm 2.82$ | 0.75 | 19.61 | -13.95 | |
| Spinal Cord $D_{max}$ | $21.44 \pm 10.02$ | $20.76 \pm 11.92$ | 0.86 | 4.02 | | 53 |
| Spinal Cord $D_{mean}$ | $2.98 \pm 2.99$ | $2.90 \pm 3.10$ | 0.08 | 2.52 | 1.53 | |
| Aorta $D_{max}$ | $26.06 \pm 27.35$ | $23.26 \pm 29.42$ | 2.80 | 10.74 | | |
| Aorta $D_{mean}$ | $5.03 \pm 7.12$ | $4.58 \pm 7.34$ | 0.45 | 8.96 | | |
| Heart $D_{max}$ | $19.63 \pm 20.63$ | $19.58 \pm 20.83$ | 0.05 | 0.25 | | 32 |
| Heart $D_{mean}$ | $4.16 \pm 5.44$ | $3.81 \pm 4.74$ | 0.35 | 8.41 | -2000.00 | |
| Average | | | 0.78 | 7.98 | | |

Table 3.4: Average percentage dose values for OARs compared to those available in Langhan *et al.* [51] and Dong *et al.* [56]. All dose values are in percent prescription dose. The improvement values are the clinical relative doses minus the $4\pi$ optimized relative dose. The normalized improvement values are calculated by dividing the improvement by the initial clinical relative dose.

| OAR | Maximum dose p-value | Mean dose p-value |
|---|---|---|
| Ipsilateral Lung | 0.40 | 0.04* |
| Contralateral Lung | 0.48 | 0.04* |
| Ipsilateral Bronchus | 0.62 | 0.67 |
| Contralateral Bronchus | 0.12 | 0.16 |
| Trachea | 0.14 | 0.07 |
| Esophagus | 0.09 | 0.07 |
| Spinal Cord | 0.48 | 0.62 |
| Aorta | 0.16 | 0.09 |
| Heart | 0.89 | 0.12 |

Statistically significant at $p < 0.05$

Table 3.5: p-value for the change to each of the maximum and mean doses to the extra-cranial OARs as calculated by the Wilcoxon signed-rank test (N=8).

# Chapter 4

# Discussion

## 4.1 Effects of Patient-Specific Collision Zones on $4\pi$ SRS

Comparing the mean and max dose for the cranial patients' OARs (N=8) showed that shifting from a general collision zone to a patient-specific collision zone did not result in significant changes as determined by the Wilcoxon rank-sum test ($p > 0.05$). The only exceptions are in the maximum dose to the right eye (p=0.017), which saw an 8% decrease in normalized dose, and the mean dose to the chiasm (p=0.034), which saw a 0.8% increase in normalized dose. The decrease in dose to the right eye is mostly likely due to majority of the PTVs being on the right side of the patient population. Thus, the right eye required increased prioritization during VMAT optimization leading to an increased volatility in dose. This in conjunction with the relative inexperience (less than one year) of the planner have could lead to this change. The change in mean dose to the chiasm could be accounted for by the small volume of the chiasm, thus any change in dose to the chiasm volume will result in a large change to the mean dose. It is important to note that the while the maximum dose to the right eye did decrease in every patient, the largest decrease in a single patient was from 10.4% to 9.1% of the prescribed dose. This will most likely have very little biological effect as the dose received by the eye was already below clinical significance.

The change to the PTV conformity index was determined to be statistically insignificant. This is unsurprising as the plans were VMAT optimized and one of the key functions of optimization is assuring dose conformity of the PTV.

The overlap scores were statistically significantly different (p=0.017). This could be due the difference in collision zone shape forcing the $4\pi$ trajectories to vary, thus varying the score. The average percentage change to the overlap score was a 5% decrease when the patient-specific collision zones were applied, which indicates that while the overlap score has been affected by the use of the patient-specific collision zone, it has not dramatically effected dose to the OARs.

Most importantly, it was shown that using a singular general collision zone is insufficient for clinical applications. When overlaying the treatment arcs calculated using the general collision zones on the patient-specific collision zones, the treatment arcs overlapped the collision zones for seven of the eight patients. This indicated if the general treatment arcs were delivered, a collision would have occurred on the unit. This emphasizes that patient-specific collision zones are essential for the safe delivery of non-coplanar radiation therapy even for cranial treatments when the patient dose not occupy a large portion of the $4\pi$ sphere or that significantly larger buffer zones are required if a general collision zone map is being used.

## 4.2 Collision Detection Accuracy

When comparing the results of the cranial detection algorithm to the work which most closely matches in both algorithm and testing methodology, Mann *et al.* [71], we see very similar results. This is illustrated in Table 3.2, where both Mann *et al.* and our sensitivity and NPV values reach unity. Additionally, our accuracy values fall within the range of accuracy values reported by Mann *et al.* By utilizing data collected directly from the patient's CT scan, both of these methodologies avoid the expense of additional equipment and increased scanning times. Whereas Mann *et al.* expands the patient contour by registering the contour of a phantom to the patient's CT, our work extends the inferior portion of the patient's CT to account for the patients torso. Extending the patient contour better accounts for the variation in patient form in comparison to using generalized anthropomorphic phantoms.

Arguably the most important ROC value to take into consideration is the negative predictive value (NPV), which goes to unity when no false negatives have occurred. The results of the cranial end-to-end testing was that the NPV was 99.99%. This indicates that using a 3 cm buffer is sufficient to assure safe cranial treatment delivery, the same result determined by Mann *et al.* [71]. Sensitivity, which indicates what percentage of the collision have been detected, we achieved 99.99% sensitivity. The accuracy of the end-to-end test refers to how close to the truth the collision detection algorithm is to real life. The accuracy of the end-to-end test was found to be 97.8%. It is important to note two factors that will affect this result. Firstly, the collision detection algorithm does not evenly sample the $4\pi$ space. The $4\pi$ sphere is projected onto the two dimensional couch-gantry map, where the top row of the overlap map represents every combination of couch position when the gantry is at 180°, and this relates to a singular point on the $4\pi$ sphere. Thus the "true" values are inflated as a single "true" match is repeated. Secondly, the couch base collision zones are based off measurements taken during the end-to-end testing. This again increases the "true" values artificially.

The reason we did not reach unity for either NPV or sensitivity is the two false negatives that were found during the accuracy testing. Both collision zones were measured with a 3 cm buffer, so an error in the collision detection process could have been propagated forward. Neither of these false negatives activated the Varian Truebeam Stx's built in collision prevention system. They may have been caused by the limitations of the voxel size of the CT system, which is 1.2 mm in the x- and y- dimensions and 2.5 mm in the z-dimension. Additionally, the phantom was arranged using image-guidance, but the head was disconnected from the body and thus there may have been small discrepancies in set-up between simulation and "treatment".

In regards to expanding this algorithm to extra-cranial cases, it was important to prove the accuracy of the collision detection portion of the algorithm. Because the extra-cranial collision detection algorithm did not receive end-to-end testing, it must be tested as two separate components: the registration and collision detection algorithms. Thus having proven the accuracy of the collision detection algorithm is equitable to the current standard within the literature, we can go on to analyze the accuracy of the registration software.

## 4.3 Registration Accuracy

Due to the nature of the registration system, there are some key limitations. The patient library size is currently quite limited when compared to the variation in patient positioning. Variation in a patient's mobility, height, and body composition results in no two patient positions being the same. Increasing the library size by acquiring more patient scans will account for these variations. But, there will always be patients which are unique cases and the current methodology is not prepared to account for this. For example, Patient 3, who consistently had the worst ROC values, compared to all other patients, as shown in Table 3.3, was the only one of the tested patients who did not use a wingboard. Thus only one scan in the library closely matched the patient positioning, resulting in the poor ROC values as the patient was an outlier.

From the ROC analysis, the trade-off between accuracy and NPV becomes clear. An NPV of unity is desired as this indicates no false negatives, which would allow the avoidance of all possible collisions. But the increase in NPV corresponds to a decrease in accuracy. Increasing the buffer results in fewer false negatives, but more false positives, limiting the the navigatable $4\pi$ space. While the 6 cm buffer produces the NPV value closest to unity (98.74 ± 1.55%), it also produces the lowest accuracy values ( 86.29 ± 2.38%). The consensus within the literature [68, 70, 71, 73] is that achieving a NPV of unity is essential to assure safe treatment delivery, thus a 6 cm buffer size, or greater, is recommended. This also accounts for the shifts in patient positioning that will occur as a consequence of image-guidance.

While the larger buffer results in the appropriate NPV of unity, it leads to a decrease in accuracy. This is clearly shown in Figure 3.4, the ROC plot. The results cluster together, trending to a higher true positive ratio and higher false positive ratio as the buffer size increases. As the buffer size increases, the collision zones expand outwards, this results in a greater percentage of positives, both true and false. The larger buffer size is required to account for the disparity between the patient's actual anatomy and the full-body scan used to represent it.

While many other studies [63, 64, 73, 74] exist which examine extra-cranial collision zones they, utilized exclusively phantoms. Currently two studies have focused on extra-cranial patient-specific collision zones. A 3 cm buffer was found to be sufficient by Miao *et al.* [70] who utilized a cylinder of acceptance imported into the treatment planning system. But the methodology fails to address the portions of the patient not captured in the CT scan. So while the collision detection methodology may open up a greater amount of treatment space, it is not sufficient for clinical applications if it fails to account for the full patient anatomy. Cardan *et al.* [68] captured the full patient anatomy using multiple depth cameras, but found it necessary to use a 6 cm buffer to achieve a NPV of unity for all five test patients. Because each patient's unique body contour is captured, Cardan *et al.* demonstrated improved accuracy results (91.50%) compared to those seen within our study.

## 4.4 Comparison of Conventional and Optimized Trajectories for SBRT

When averaged across all patients (N=8), no statistically significant change in dose was found, outside of the change in mean dose to the lungs, when comparing the conventional and $4\pi$ optimized trajectories. The Wilcoxon signed-rank test indicated that the null hypothesis could not be rejected for the majority of the OARs, and the p-values are displayed in Table 3.5. The only significant (p=0.04) change in dose to OARs was the mean dose to the ipsilateral and contralateral lungs. Despite the large error bars, it is interesting to note that the majority of the OARs saw a mean decrease in mean and maximum dose. The ipsilateral lung mean dose increased by 0.71%. Considering the ipsilateral lung was not included in the overlap map calculation, this was not unexpected. In both plans during the treatment planning optimization, the ipsilateral lung had optimization objectives. This increase in dose is most likely due to the increased number of beamlets passing through the lung of the patients. In the conventional trajectory plan, the treatment template had two 190° arcs delivered to the ipsilateral side of the patient. During the creation of the $4\pi$ trajectories, it is planned for the gantry to span the maximum, safe, amount of a 360° delivery arc, and results in a need to push a greater amount of photons to reach the PTV within the ipsilateral lung as the treatment head rotates towards the contralateral side of the patients. This could result in a larger mean dose to the ipsilateral lung. The contralateral lung saw a 0.55% decrease in mean dose, which was determined to be statistically significant ($p=0.04$). This is potentially due to the $4\pi$ algorithm taking the contralateral lung into consideration. More likely is that the collision zones block the majority of the treatment angles which would result in the treatment beam passing through the contralateral lung. Additionally, while the changes in dose were statistically significant, the initial dose values were already below clinically significant dose values as they had been optimized for clinical delivery. Examining the conformity index, no statistically significant change was found ($p=0.13$); this is ideal as the application of $4\pi$ should not compromise the PTV coverage.

No statistical significance was found for the change in dose for the majority of OARs. This may be due to two factors: the small sample size or the need to further optimize the $4\pi$ algorithim. Rejecting the theory that there is no benefit to apply $4\pi$ to SBRT patients is validated by the following three points. Firstly, when calculating the normalized improvement (Table 3.4) some notable values result, such as the 25.89% decrease in the mean dose to the contralateral bronchus. Secondly, the reduction in overlap score has a few implications. Reducing the overlap score means that the VMAT optimization algorithm should have an easier time optimizing the treatment plan as the arcs have been optimized to avoid the OARs. And so, while no dosimeteric improvements to the OARs were seen, the improvement in overlap score indicates that the $4\pi$ algorithm has the potential to reduce planning time.

Thirdly, the current $4\pi$ optimization algorithm was developed for cranial cases. There are several notable differences between SBRT and SRS/SRT cases. Most evident is the size difference and variance of the OARs. In cranial cases, the OARs are similarly sized and relatively small. In SBRT, lung OARs vary widely in size with lungs being comparatively massive to the other OARs and the PTV itself. This leads to the larger organs like the contralateral lung "washing out" other organs as it dominates a larger area of the overlap map. Integrating organ-specific weighting values to the generation of the overlap map, such as those used by MacDonald and Thomas [41], would help address this issue. The algorithm also seeks to navigate the map from top to bottom, a full 360° arc span. If the algorithm was limited to navigate a 190° on the ipsilateral side, as is the clinical standard, the resulting dose to OARs will be at least equal to if not superior to the clinical plan as the beam will navigate through a smaller portion of the patient's contralateral side and will be better $4\pi$ optimized to avoid overlap with OARs.

At the time of writing, only two research papers [51, 56] have been published which examine applying $4\pi$ to lung SBRT. Langhans *et al.* [51] created an algorithm designed to calculate dynamic treatment trajectories called NoVo (Noncoplanar VMAT optimization). The reported results for the singular lung case tested are presented in Table 3.4. Collision zones were manually selected, although it is unclear how these coordinate combinations were selected. When comparing the dosimeteric results, it is important to note that the normalized improvement values presented are for the average values for eight patients in our work and a single patient in Langhan *et al.*'s work. While the normalized improvement in mean dose to the lungs is far greater in Langhan *et al.*'s work, 18.85% for the contralateral lung and 42.86% for the ipsilatereal lung, compared to the results achieved in our work, −8.10% for the contralateral lung and 27.50% for the ipsilateral lung, the remaining OAR value improvements reported are lower then those achieved in our work. Dong *et al.* [56] evaluted 12 lung SBRT patients who had previously been treated with IMRT. Their $4\pi$ algorithm determined optimized non-coplanar IMRT plans with up to 30 beams, and the improvements in dose to OARs is displayed in Table 3.4. The dosimeteric improvements are superior to the results achieved using our methodology, but Dong *et al.*'s results were not created with clinical deliverability as a consideration. For each of the IMRT beams, the couch will need to be rotated which will require a therapist to enter the room to rotate the couch, this will lead to significantly longer treatment times compared to the VMAT plans. The difficulty that comes with comparing the results of these two papers [51, 56] to our work is the variance between the delivery techniques, static $4\pi$ vs. NOVO vs. non-coplanar VMAT, and our focus on the treatment plans being deliverable with the current available technology. Although, it is encouraging to see that extra-cranial dedicated optimization algorithms can produce excellent dosimeteric results.

# Chapter 5

# Conclusion and Future Work

## 5.1 Conclusion

A new methodology of determining patient-specific collision zones has been presented. It has been shown that applying patient-specific collision zones for cranial $4\pi$ radiation therapy, in place of using a singular general collision zone, does not impact the dosimeteric results. Additionally, the value of patient-specific collision zones was emphasized by the revelation that the majority of the test patients would see a collision had the general collision zone been used. To safely apply $4\pi$ SRS/SRT methodology, patient-specific collision zones must be used. The safety of these trajectories was confirmed by comparing the generated patient-specific collision zones to actual patient collision zones with an end-to-end test. The results of this analysis showed that using a 3 cm buffer results in a NPV of unity, which is essential for safe delivery. During this testing, the couch base collision zone was encountered and measured. The results of the end-to-end testing enabled the accuracy testing of the SBRT registration algorithm.

The results of the registration accuracy testing showed that a 6 cm safety margin, at least, is required to generate safe collision zones, the same as the most comprehensive methodology current present in the literature [68]. While this larger buffer results in the appropriate NPV of unity, it leads to a decrease in accuracy. While the current methodology is sufficient, ideally further improvement would allow maintaining high NPV values while improving accuracy values. Increasing the accuracy will increase the number of available treatment angles by shrinking collision zones.

Applying $4\pi$ to lung SBRT patients resulted in no notable dosimeteric improvements. Considering that the $4\pi$ algorithm utilized was not designed or optimized for extra-cranial patients, this is not surprising. The results achieved by other research groups working with specialized extra-cranial algorithms show the potential of $4\pi$ SBRT. But, these works have yet to apply patient-specific collision zones. The synthesis of these two concepts will result in safe $4\pi$ delivery with decreased dose to OARs.

## 5.2 Future Work

From the results of our study, we can conclude that it is possible to accurately determine patient-specific collision zones for both cranial and extra-cranial patients. However, two areas which could benefit from improvement are evident. Firstly, the registration algorithm would benefit from an increase in accuracy. This can be achieved in two ways, by either moving towards a system similar to that outlined by Cardan *et al.* [68] in which every patient is scanned, or by expanding the patient scan library to better capture the patient population and allowing for more choices in body contour selection. By examining the height and weight distribution of patients, a library size which would cover a high percentile of patient cases could be determined. Both of these methods would require additional clinical work to either prepare the scanning equipment or assess the required size of, and then build the library. Secondly, as previously mentioned, the $4\pi$ algorithm must be modified to better suit extra-cranial geometries. This will require determining organ-specific weighting factors and incorporating a foreground/background factor, as well as take into account the large size differential between many of the OARs and the PTV. Work is currently in progress to optimize the $4\pi$ algorithm for extra-cranial purposes.

For the purpose of a future manuscript and to improve the robustness of the statistical analysis, more lung patients will be planned using the $4\pi$ SBRT methodology. Furthermore, this study was limited to lung patients, and in line with other groups, it would be valuable to study other treatment sites such as the liver, spine, and prostate. Studying these sites will require similar adjustments as those listed for the improvement of lung SBRT $4\pi$. For example, liver patients are treated without the wing-board, thus the current patient library would be insufficient as the majority of the patients scanned used a wing-board.

# Bibliography

[1] Canadian Cancer Statistics Advisory Committee. Canadian Cancer Statistics 2018, [Online]. Available: http://www.cancer.ca/en/cancer-information/cancer-101/canadian-cancer-statistics-publication [2018,October,15]. Canadian Cancer Statistics Advisory Committee, Toronto, ON., 2018.

[2] A. V. Louie, G. B. Rodrigues, D. A. Palma, and S. Senan, "Measuring the population impact of introducing stereotactic ablative radiotherapy for stage i non-small cell lung cancer in canada," *The Oncologist*, vol. 19, no. 8, pp. 880–885, 2014.

[3] E. Podgorsak, *Radiation Physics for Medical Physicists.* Biological and Medical Physics, Biomedical Engineering, Springer Berlin Heidelberg, 2010.

[4] *Radiation Oncology Physics: A Handbook for Teachers and Students.* Non-serial Publications, Vienna: INTERNATIONAL ATOMIC ENERGY AGENCY, 2005.

[5] E. Zeman, E. Schreiber, and J. Tepper, "Basics of radiation therapy," pp. 393–422, 01 2013.

[6] K. N. Kielar, E. Mok, A. Hsu, L. Wang, and G. Luxton, "Verification of dosimetric accuracy on the truebeam stx: Rounded leaf effect of the high definition mlc," *Medical Physics*, vol. 39, no. 10, pp. 6360–6371, 2012.

[7] S. Takahashi, "Conformation radiotherapy-rotation techniques as applied to radiography and radiotherapy of cancer," *Acta Radiol*, vol. 242, pp. 1–142, 1965.

[8] K. Otto, "Volumetric modulated arc therapy: Imrt in a single gantry arc," *Medical Physics*, vol. 35, no. 1, pp. 310–317, 2008.

[9] Z. C. Taskin, J. C. Smith, H. E. Romeijn, and J. F. Dempsey, "Optimal multileaf collimator leaf sequencing in imrt treatment planning," *Oper. Res.*, vol. 58, pp. 674–690, 2010.

[10] E. H. Balagamwala, S. T. Chao, and J. H. Suh, "Principles of radiobiology of stereotactic radiosurgery and clinical applications in the central nervous system," *Technology in Cancer Research & Treatment*, vol. 11, no. 1, pp. 3–13, 2012.

[11] L. L., "A stereotaxic apparatus for intracerebral surgery," *Acta Chir Scand*, vol. 99, pp. 229–233, 1947.

[12] L. L., “The stereotactic method and radiosurgery of the brain,” *Acta Chir Scand*, vol. 102, pp. 316–319, 1951.

[13] C.-K. Park and D. G. Kim, “Historical background.,” *Progress in neurological surgery*, vol. 25, pp. 1–12, 2012.

[14] L. Leksell, *Stereotaxis and radiosurgery: an operative system.* Thomas, 1971.

[15] L. D. Lunsford, J. Flickinger, G. Lindner, and A. Maitz, “Stereotactic radiosurgery of the brain using the first united states 201 cobalt-60 source gamma knife,” *Neurosurgery*, vol. 24, p. 151–159, Feb 1989.

[16] D. P. Cordeiro and D. J. Schlesinger, *Leksell Gamma Knife Radiosurgery*, pp. 55–65. Cham: Springer International Publishing, 2019.

[17] L. Steiner, C. P. Yen, J. Jagannathan, D. Schlesinger, and M. Steiner, *Gamma Knife: Clinical Aspects*, pp. 1037–1086. Berlin, Heidelberg: Springer Berlin Heidelberg, 2009.

[18] D. V. Betti O, “Irradiation stereotaxique multifasceaux,” *Neurochirurgie*, vol. 29, pp. 295–298, 1983.

[19] K. R. Winston and W. Lutz, “Linear Accelerator as a Neurosurgical Tool for Stereotactic Radiosurgery,” *Neurosurgery*, vol. 22, pp. 454–464, 03 1988.

[20] L. W., W. K., and M. N., “A system for stereotactic radiosurgery with a linear accelerator,” *International journal of radiation oncology, biology, physics*, vol. 14 2, pp. 378–381, 1988.

[21] J. R. A. Jr., S. D. Chang, M. J. Murphy, J. Doty, P. Geis, and S. L. Hancock, “The cyberknife: A frameless robotic system for radiosurgery,” *Stereotactic and Functional Neurosurgery*, vol. 69, no. 1-4, p. 124–128, 1997.

[22] I. Gibbs, “Frameless image-guided intracranial and extracranial radiosurgery using the cyberknife™ robotic system,” *Cancer/Radiothérapie*, vol. 10, p. 283–287, Sep 2006.

[23] V. Kearney, J. P. Cheung, C. Mcguinness, and T. D. Solberg, “Cyberarc: a non-coplanar-arc optimization algorithm for cyberknife,” *Physics in Medicine and Biology*, vol. 62, p. 5777–5789, Jun 2017.

[24] *https://www.accuray.com/cyberknife-system-lp/.*

[25] S. H. Benedict, K. M. Yenice, D. Followill, J. M. Galvin, W. Hinson, B. Kavanagh, P. Keall, M. Lovelock, S. Meeks, L. Papiez, T. Purdie, R. Sadagopan, M. C. Schell, B. Salter, D. J. Schlesinger, A. S. Shiu, T. Solberg, D. Y. Song, V. Stieber, R. Timmerman, W. A. Tomé, D. Verellen, L. Wang, and F.-F. Yin, “Stereotactic body radiation therapy: The report of aapm task group 101,” *Medical Physics*, vol. 37, no. 8, pp. 4078–4101, 2010.

[26] A. Hamilton, B. Lulu, H. Fosmire, B. Stea, J. Cassady, W. Friedman, and R. Nockels, “Preliminary clinical experience with linear accelerator-based spinal stereotactic radiosurgery,” *Neurosurgery*, vol. 36, no. 2, pp. 311–319, 1995.

[27] H. Blomgren, I. Lax, I. Näslund, and R. Svanström, “Stereotactic high dose fraction radiation therapy of extracranial tumors using an accelerator: Clinical experience of the first thirty-one patients,” *Acta Oncologica*, vol. 34, no. 6, p. 861–870, 1995.

[28] R. I. Whyte, R. Crownover, M. J. Murphy, D. P. Martin, T. W. Rice, M. M. Decamp, R. Rodebaugh, M. S. Weinhous, and Q.-T. Le, “Stereotactic radiosurgery for lung tumors: preliminary report of a phase i trial,” *The Annals of Thoracic Surgery*, vol. 75, p. 1097–1101, Apr 2003.

[29] S. Dieterich, C. Cavedon, C. F. Chuang, A. B. Cohen, J. A. Garrett, C. L. Lee, J. R. Lowenstein, M. F. d’souza, D. D. Taylor Jr., X. Wu, and C. Yu, “Report of aapm tg 135: Quality assurance for robotic radiosurgery,” *Medical Physics*, vol. 38, no. 6Part1, pp. 2914–2936, 2011.

[30] *Accuray tracking vest used to track respiratory motion.* Accuray.

[31] Y. Kamino, K. Takayama, M. Kokubo, Y. Narita, E. Hirai, N. Kawawda, T. Mizowaki, Y. Nagata, T. Nishidai, and M. Hiraoka, “Development of a four-dimensional image-guided radiotherapy system with a gimbaled x-ray head,” *International Journal of Radiation Oncology, Biology, Physics*, vol. 66, no. 1, pp. 271–278, 2006.

[32] M. Burghelea, D. Verellen, K. Poels, T. Gevaert, T. Depuydt, K. Tournel, C. Hung, V. Simon, M. Hiraoka, and M. de Ridder, “Geometric verification of dynamic wave arc delivery with the vero system using orthogonal x-ray fluoroscopic imaging,” *International Journal of Radiation Oncology, Biology, Physics*, vol. 92, no. 4, pp. 754–761, 2015.

[33] E. Hall and A. Giaccia, *Radiobiology for the Radiologist.* Wolters Kluwer Health, 2018.

[34] S. M. Harding, R. P. Hill, and R. G. Bristow, *CHAPTER 15. Molecular and Cellular Basis of Radiotherapy.* The McGraw-Hill Companies, Inc., 5 ed., 2013.

[35] E. H. Balagamwala, S. T. Chao, and J. H. Suh, “Principles of radiobiology of stereotactic radiosurgery and clinical applications in the central nervous system,” *Technology in Cancer Research & Treatment*, vol. 11, no. 1, pp. 3–13, 2012.

[36] J. Tanksley, J. K. Salama, and J. P. Kirkpatrick, *Rationale for Fractionated SRS and Single SRS Session Approaches*, pp. 31–40. Cham: Springer International Publishing, 2019.

[37] G. M. Videtic, J. Donington, M. Giuliani, J. Heinzerling, T. Z. Karas, C. R. Kelsey, B. E. Lally, K. Latzka, S. S. Lo, D. Moghanaki, and et al., "Stereotactic body radiation therapy for early-stage non-small cell lung cancer: Executive summary of an astro evidence-based guideline," *Practical Radiation Oncology*, vol. 7, no. 5, p. 295–301, 2017.

[38] D. Andrews, C. Scott, P. Sperduto, A. Flanders, L. Gaspar, M. Schell, M. Werner-Wasik, W. Demas, J. Ryu, J.-P. Bahary, L. Souhami, M. Rotman, M. Mehta, and W. Curran, "Whole brain radiation therapy with or without stereotactic radiosurgery boost for patients with one to three brain metastases: Phase iii results of the rtog 9508 randomised trial," *Lancet*, vol. 363, pp. 1665–72, 06 2004.

[39] G. Videtic, C. Hu, A. Singh, J. Chang, W. Parker, K. Olivier, S. Schild, R. Komaki, J. Urbanic, and H. Choy, "Nrg oncology rtog 0915 (ncctg n0927): A randomized phase ii study comparing 2 stereotactic body radiation therapy (sbrt) schedules for medically inoperable patients with stage i peripheral non-small cell lung cancer," *International journal of radiation oncology, biology, physics*, vol. 93, pp. 757–764, 11 2015.

[40] Y. Yang, P. Zhang, L. Happersett, J. Xiong, J. Yang, M. Chan, K. Beal, G. Mageras, and M. Hunt, "Choreographing Couch and Collimator in Volumetric Modulated Arc Therapy," *International Journal of Radiation Oncology*Biology*Physics*, vol. 80, no. 4, pp. 1238 – 1247, 2011.

[41] R. Lee Macdonald and C. G. Thomas, "Dynamic trajectory-based couch motion for improvement of radiation therapy trajectories in cranial SRT," *Medical Physics*, vol. 42, no. 5, pp. 2317–2325, 2015.

[42] R. L. Macdonald, J. L. Robar, and C. G. Thomas, "Overlap-guided fixed-patient support positioning optimization for cranial srt.," *Medical physics*, vol. 44 1, pp. 17–27, 2017.

[43] K. Woods, T. B. Kaprealian, P. Lee, and K. Sheng, "Cochlea-sparing acoustic neuroma treatment with $4\pi$ radiation therapy," *International Journal of Radiation Oncology, Biology, Physics*, vol. 99, no. 2, pp. E739–E739, 2017.

[44] D. Nguyen, J.-C. M. Rwigema, V. Y. Yu, T. Kaprealian, P. Kupelian, M. Selch, P. Lee, D. A. Low, and K. Sheng, "Feasibility of extreme dose escalation for glioblastoma multiforme using $4\pi$ radiotherapy," *Radiation oncology (London, England)*, vol. 9, no. 1, p. 239, 2014.

[45] V. Y. Yu, A. Landers, K. Woods, D. Nguyen, M. Cao, D. Du, R. K. Chin, K. Sheng, and T. B. Kaprealian, "A prospective $4\pi$ radiation therapy clinical study in recurrent high-grade glioma patients," *International Journal of Radiation Oncology, Biology, Physics*, vol. 101, no. 1, pp. 144–151, 2018.

[46] V. L. Murzin, K. Woods, V. Moiseenko, R. Karunamuni, K. R. Tringale, T. M. Seibert, M. J. Connor, D. R. Simpson, K. Sheng, and J. A. Hattangadi-Gluth, “$4\pi$ plan optimization for cortical-sparing brain radiotherapy,” *Radiotherapy and Oncology*, vol. 127, no. 1, pp. 128–135, 2018.

[47] D. Papp, T. Bortfeld, and J. Unkelbach, “A modular approach to intensity-modulated arc therapy optimization with noncoplanar trajectories,” *Physics in medicine and biology*, vol. 60, no. 13, pp. 5179–5198, 2015.

[48] P. Dong, P. Lee, D. Ruan, T. Long, E. Romeijn, Y. Yang, D. Low, P. Kupelian, and K. Sheng, “$4\pi$ Non-Coplanar Liver SBRT: A Novel Delivery Technique,” *International Journal of Radiation Oncology*Biology*Physics*, vol. 85, no. 5, pp. 1360 – 1366, 2013.

[49] Q. Lyu, V. Y. Yu, D. Ruan, R. Neph, D. O’Connor, and K. Sheng, “A novel optimization framework for VMAT with dynamic gantry couch rotation,” *Physics in Medicine & Biology*, vol. 63, p. 125013, jun 2018.

[50] A. Landers, D. O’Connor, D. Ruan, and K. Sheng, “Automated $4\pi$ radiotherapy treatment planning with evolving knowledge-base,” *Medical Physics*, vol. 46, no. 9, pp. 3833–3843, 2019.

[51] M. Langhans, J. Unkelbach, T. Bortfeld, and D. Craft, “Optimizing highly noncoplanar vmat trajectories: the novo method,” *Physics in medicine and biology*, vol. 63, no. 2, p. 025023, 2018.

[52] G. Smyth, J. C. Bamber, P. M. Evans, and J. L. Bedford, “Trajectory optimization for dynamic couch rotation during volumetric modulated arc radiotherapy,” *Physics in medicine and biology*, vol. 58, no. 22, pp. 8163–8177, 2013.

[53] P. Liang, Jieming, P. Atwood, Todd, M. von Eyben, Rie, P. Fahimian, Benjamin, P. Chin, Erika, M. Horst, Kathleen, P. Otto, Karl, and P. Hristov, Dimitre, “Trajectory modulated arc therapy: A fully dynamic delivery with synchronized couch and gantry motion significantly improves dosimetric indices correlated with poor cosmesis in accelerated partial breast irradiation,” *International Journal of Radiation Oncology, Biology, Physics*, vol. 92, no. 5, pp. 1148–1156, 2015.

[54] B. Woods, Kaley, B. Nguyen, Dan, B. Tran, Angelia, B. Yu, Victoria Y., P. Cao, Minsong, P. Niu, Tianye, M. Lee, Percy, and P. Sheng, Ke, “Viability of noncoplanar vmat for liver sbrt compared with coplanar vmat and beam orientation optimized $4\pi$ imrt,” *Advances in Radiation Oncology*, vol. 1, no. 1, pp. 67–75, 2016.

[55] J. Ng, D. P. Horowitz, P. Yan, M. Schweizer, W. Feng, K. Chao, D. J. Brenner, T. K. Hei, I. Shuryak, and S. Cheng, “Comparing lung dosimetry and

secondary malignancy risks associated with stereotactic body radiation therapy (sbrt) using intensity modulated radiation therapy (imrt), coplanar volumetric modulated arc therapy (vmat), and noncoplanar volumetric modulated arc therapy techniques," *International Journal of Radiation Oncology, Biology, Physics*, vol. 84, no. 3, pp. S588–S588, 2012.

[56] P. Dong, P. Lee, D. Ruan, T. Long, E. Romeijn, D. A. Low, P. Kupelian, J. Abraham, Y. Yang, and K. Sheng, "$4\pi$ Noncoplanar Stereotactic Body Radiation Therapy for Centrally Located or Larger Lung Tumors," *International Journal of Radiation Oncology*Biology*Physics*, vol. 86, no. 3, pp. 407 – 413, 2013.

[57] M. L. Kessler, D. L. McShan, and B. A. Fraass, "A computer-controlled conformal radiotherapy system. III: Graphical simulation and monitoring of treatment delivery," *International Journal of Radiation Oncology*Biology*Physics*, vol. 33, no. 5, pp. 1173 – 1180, 1995.

[58] J. L. Humm, D. Pizzuto, E. Fleischman, and R. Mohan, "Collision detection and avoidance during treatment planning," *International Journal of Radiation Oncology*Biology*Physics*, vol. 33, no. 5, pp. 1101 – 1108, 1995.

[59] C. Hua, J. Chang, K. Yenice, M. Chan, and H. Amols, "A practical approach to prevent gantry–couch collision for linac-based radiosurgery," *Medical Physics*, vol. 31, no. 7, pp. 2128–2134, 2004.

[60] H. Deng and S. Li, "Su-gg-t-529: Fully automated patient specific collision check for novalis radiosurgery system," *Medical Physics*, vol. 37, no. 6Part24, pp. 3308–3308, 2010.

[61] M. F. Tsiakalos, E. Schrebmann, K. Theodorou, and C. Kappas, "Graphical treatment simulation and automated collision detection for conformal and stereotactic radiotherapy treatment planning," *Medical Physics*, vol. 28, no. 7, pp. 1359–1363, 2001.

[62] B. Ye, Q. Tang, J. Yao, and W. Gao, "Collision-free path planning and delivery sequence optimization in noncoplanar radiation therapy," *IEEE Transactions on Cybernetics*, vol. 49, no. 1, pp. 42–55, 2019.

[63] V. Y. Yu, A. Tran, D. Nguyen, M. Cao, D. Ruan, D. A. Low, and K. Sheng, "The development and verification of a highly accurate collision prediction model for automated noncoplanar plan delivery," *Medical Physics*, vol. 42, no. 11, pp. 6457–6467, 2015.

[64] C. Jenkins, L. Xing, and A. Yu, "Using a handheld stereo depth camera to overcome limited field-of-view in simulation imaging for radiation therapy treatment planning," *Medical Physics*, vol. 44, no. 5, pp. 1857–1864, 2017.

[65] Max M. Chao, Liang S. Chao, Yu J. Chen, Chuen M. Hsieh, Shueh C. Liou, Yuh L. Lee, and Sang H. Yen, "Image Display for Collision Avoidance of Radiation Therapy: Treatment Planning," *Journal of Digital Imaging*, vol. 14, pp. 186–191, Dec. 2001.

[66] S. J. Becker, "Collision indicator charts for gantry-couch position combinations for varian linacs," *Journal of Applied Clinical Medical Physics*, vol. 12, no. 3, pp. 16–22, 2011.

[67] W. Zou, H. Lin, J. P. Plastaras, H. Wang, V. Bui, N. Vapiwala, J. McDonough, Z. Tochner, and S. Both, "A clinically feasible method for the detection of potential collision in proton therapy," *Medical Physics*, vol. 39, no. 11, pp. 7094–7101, 2012.

[68] R. A. Cardan, R. A. Popple, and J. Fiveash, "A priori patient-specific collision avoidance in radiotherapy using consumer grade depth cameras," *Medical Physics*, vol. 44, no. 7, pp. 3430–3436, 2017.

[69] V. Suriyakumar, R. Xu, C. Pinter, and G. Fichtinger, "Open-source software for collision detection in external beam radiation therapy," p. 101351G, 03 2017.

[70] J. Miao, C. Niu, Z. Liu, Y. Tian, and J. Dai, "A practical method for predicting patient-specific collision in radiotherapy," *Journal of Applied Clinical Medical Physics*, 2020.

[71] T. D. Mann, N. P. Ploquin, W. R. Gill, and K. S. Thind, "Development and clinical implementation of eclipse scripting-based automated patient-specific collision avoidance software," *Journal of Applied Clinical Medical Physics*, vol. 0, no. 0, 2019.

[72] L. Padilla, E. A. Pearson, and C. A. Pelizzari, "Collision prediction software for radiotherapy treatments," *Medical Physics*, vol. 42, no. 11, pp. 6448–6456, 2015.

[73] N. Islam, J. Kilian-Meneghin, S. deBoer, and M. Podgorsak, "A collision prediction framework for noncoplanar radiotherapy planning and delivery," *Journal of Applied Clinical Medical Physics.*

[74] E. Nioutsikou, J. L. Bedford, and S. Webb, "Patient-specific planning for prevention of mechanical collisions during radiotherapy," *Physics in Medicine and Biology*, vol. 48, pp. N313–N321, Oct. 2003.

[75] Aniwaa, "Creaform go!scan 50 review - professional portable 3d scanner," Jul 2014.

[76] "The sbrt solution," Oct 2016.

[77] W. by Today's Veterinary Business in November 2019, "Varian radiotherapy units coming to vca cancer centers," Nov 2019.

[78] P. J. Besl and N. D. McKay, "A method for registration of 3-d shapes," *IEEE Transactions on Pattern Analysis and Machine Intelligence*, vol. 14, pp. 239–256, Feb 1992.

[79] K. K.an, "Varian truebeam linear accelerator radiotherapy system: 3d model."

[80] M. Pharr, W. Jakob, and G. Humphreys, *Physically based rendering: from theory to implementation.* Morgan Kaufmann Publishers/Elsevier, 2017.

[81] S. Han, "Towards Efficient Implementation of an Octree for a Large 3d Point Cloud.," *Sensors (Basel, Switzerland)*, vol. 18, no. 12, 2018.

[82] S. Gottschalk, M. C. Lin, and D. Manocha, "Obbtree: A hierarchical structure for rapid interference detection," in *Proceedings of the 23rd annual conference on Computer graphics and interactive techniques*, pp. 171–180, Citeseer, 1996.

[83] J. C. T. Chen, D. M. Bugoci, M. R. Girvigian, M. J. Miller, A. Arellano, and J. Rahimian, "Control of brain metastases using frameless image-guided radiosurgery," *Neurosurgical Focus FOC*, vol. 27, no. 6, p. E6, 2009.

[84] T. Landberg, J. Chavaudra, J. Dobbs, J. P. Gerard, G. Hanks, J. C. Horiot, K. A. Johansson, T. Möller, J. Purdy, N. Suntharalingam, and H. Svensson, "Report 62," *Journal of the International Commission on Radiation Units and Measurements*, vol. os32, pp. NP–NP, 04 2016.

[85] K. R. Hutson, T. L. Schlosser, and D. R. Shier, "On the distributed bellman-ford algorithm and the looping problem.," *INFORMS Journal on Computing*, vol. 19, no. 4, pp. 542 – 551, 2007.